

# Multiscale modeling of discontinuous dynamic recrystallization during hot working by coupling multilevel cellular automaton and finite element method

Fei Chen<sup>a, 1\*</sup>, Huajia Zhu<sup>b</sup>, Wen Chen<sup>c</sup>, Hengan Ou<sup>d</sup>, Zhenshan Cui<sup>a, \*</sup>

<sup>a</sup> National Engineering Research Center of Die and Mold CAD, Shanghai Jiao Tong University, 1954 Huashan Road, Shanghai, 200030, PR China

<sup>b</sup> Department of Mechanical Engineering, University College London, Torrington Place, London, WC1E 7JE, UK

<sup>c</sup> Altair Engineering Inc. (Shanghai), 2803 Capital Square, 268 Hengtong Road, Shanghai, 200070, PR China

<sup>d</sup> Department of Mechanical, Materials and Manufacturing Engineering, University of Nottingham, Nottingham, NG7 2RD, UK

## Abstract

Discontinuous dynamic recrystallization (dDRX) is considered an effective way to obtain fine grain microstructures during hot working of materials with low-to-medium stacking fault energy (SFE). However, to date, investigation and modeling of dDRX in complex hot working processes are not appropriately performed, which hinders further control of the microstructure and forming quality of products during hot working. In this study, a multiscale modeling framework, namely the MCAFE-dDRX model, was constructed by coupling the multilevel cellular automaton (MCA) and finite element (FE) method. The data acquired via the FE method was used as an input for MCA simulation by discretizing the increment in FE time to consider the deformation history of materials. Compared to previous studies where only the effects of constant strain rate and temperature on the deformation of materials are analysed, the MCAFE-dDRX model can evaluate the dDRX microstructure evolution at different Zener-Hollomon levels, which has been validated by hot extrusion in this study. The developed simulation framework facilitates the prediction of microstructure evolution during heterogeneous and non-isothermal deformation of materials.

## Keywords:

Microstructures

Thermomechanical processes

Metallic material

Probability and statistics

Multilevel cellular automaton

## 1. Introduction

Thermomechanical processing is an effective way to control the microstructure and grain refinement of commercial metals and alloys (Chatziathanasiou et al., 2016; Yang et al., 2020).

---

\*Corresponding authors: National Engineering Research Center of Die and Mold CAD, Shanghai Jiao Tong University, PR China.  
E-mail addresses: feichen@sjtu.edu.cn (F. Chen), cuizs@sjtu.edu.cn (Z. Cui)

During the past two decades, significant efforts have been devoted to realizing the thermomechanical processing of materials more cost-effectively. Among the various techniques, promoting the occurrence of dynamic recrystallization (DRX) is the most well-developed method to refine grains under hot working conditions (for example, hot extrusion, hot rolling, and hot forging) (Galiyev et al., 2001; McQueen, 2004; Sakai et al., 2014; Lieou and Bronkhorst 2018; Tang et al., 2019).

In the past few decades, the DRX of metals and alloys under hot working conditions has been mainly examined by theoretical and experimental studies (Sakai et al., 2014). The most comprehensive reviews on DRX have been performed by top researchers in this field (Doherty et al., 1997; Raabe, 2002; Rollett, 2004; McQueen, 2004; Sakai et al., 2014; Huang et al., 2018). It has been commonly acknowledged by both industry and academia that there are primarily two different DRX mechanisms: discontinuous DRX (dDRX) and continuous DRX (cDRX). dDRX involves the nucleation of recrystallized grains followed by long-range migration of high-angle grain boundaries (HAGBs). In materials with low-to-medium stacking fault energy (SFE), the local difference in dislocation density provides the driving force for the nucleation of new grains. Relatively dislocation-free nuclei can be formed due to the bulging of corrugated grain boundaries (Ponge and Gottstein, 1998). The new recrystallized grains are separated from the adjacent deformed matrix by HAGBs, which continue to grow into the surrounding dislocated matrix and substantially decrease the local dislocation density, finally softening the material. The term dynamic emphasizes the continuous occurrence of recrystallization during plastic deformation. Moreover, dDRX occurs in two separate stages: nucleation and growth of new undeformed grains (Sakai et al., 2014). However, as for cDRX, during the growth of new undeformed grains, competition arises between the accumulation of dislocations owing to work hardening and annihilation of dislocations caused by dynamic recovery (DRV), which is the dominant factor leading to the formation of subgrains with strain (Tsuzaki et al., 1996; Rollett et al., 2004; McQueen et al., 2004; Sun et al., 2018). As reported by Gourdet and Montheillet (2003), subgrain boundaries change from low-angle grain boundaries (LAGBs) to HAGBs, thus finally leading to the generation of new recrystallized grains with the accumulation of deformation.

In the last two decades, numerous studies have been conducted to discover an efficient way to simulate hot working with DRX (Qu et al., 2005; Lin and Dean, 2005; Fan and Yang, 2011; Puchi-Cabrera et al., 2013, 2014, 2018; Zhao et al., 2016, 2018; Cho et al., 2019; Tang et al., 2019; Lieou et al., 2019). Some pioneering studies have been reported by Sellars et al. (1985), Busso (1998), and McQueen et al. (2004) in this regard. Based on these studies, the evolutions of DRX volume fraction, DRX grain size (Lin and Liu, 2003; Lin et al., 2008), grain boundary fraction, subgrain size (Sellars and Zhu, 2000), and mobile dislocations and different types of immobile dislocations (Roters et al., 2000; Fan and Yang, 2011) were modeled and coupled as a few internal state variables (ISVs) into a constitutive model. More recently, Puchi-Cabrera et al. (2018) innovatively proposed physically-based constitutive equations for R260 steel, which undergoes both DRV and DRX during high-temperature

deformation. The corresponding model employed an appropriate differential of the Avrami equation to describe the flow stress at various Zeller-Hollomon parameters. To date, simulating the hot working with DRX by a combination of finite element (FE) and the established constitutive equations is considered an effective method. However, the success of this coupled method significantly depends on the accuracy of parameter identification. Therefore, in the past few years, research on the ISV method has been mainly focused on identifying the related parameters (Andrade-Campos et al., 2007; Qu et al., 2008; Spranghers et al., 2014), and evaluating the calculation efficiency of complex constitutive equations. Nevertheless, developing a model that can accurately describe the complex thermal and deformation histories of materials during actual hot working is particularly challenging. Furthermore, these simulations cannot provide a visible evolution of the virtual microstructure of materials during hot working with DRX.

To obtain an insight into the DRX mechanisms during hot working, other methods on a mesoscale and their combinations have also been constructed. Among them, cellular automaton (CA) is an effective way to study the DRX behavior of materials during hot working because of its high computational efficiency and flexibility. Based on the physical metallurgy principles of DRX, complex physical phenomena and morphologies can be explained by only establishing local switching rules without the need of calculating complex differential equations (Raabe, 1999, 2000; Janssens, 2003, 2010). Since the pioneering research of Goetz and Seetharaman (1998), the CA model has been attracting extensive attention and has become one of the important reach topics in the field of hot working with DRX. Ding and Guo (2001) further proposed a model based on the model constructed by Goetz and Seetharaman (1998), in which the metallurgical principles of plastic deformation and crystallographic information were considered for the first time. Janssens (2003) studied the intrinsic characteristics of a three-dimensional (3D) CA model for the first time to simulate the microstructure evolution during recrystallization and grain growth. Kugler and Turk (2004) provided the possibility of the commercial application of the CA model by clearly defining the CA time step. In addition, Xiao et al. (2008), Yazdipour et al. (2008), Zheng et al. (2008), Svyetlichnyy et al. (2010, 2014), Chen et al. (2010, 2012, 2014, 2020), and He et al. (2020) promoted the development of the theories of CA simulation of DRX from the aspects of the topological structure of grain boundaries and the discrete accuracy of the two-dimensional (2D)/3D CA model. In summary, although improved CA models and related theories for describing hot working with DRX have been proposed, most studies primarily focus on the deformation of materials under constant strain rate and temperature conditions. Moreover, practical applications of this method in actual metal forming are limited due to the intrinsic characteristics of non-uniform and non-isothermal deformation under hot working conditions.

Accordingly, some previous studies have focused on the investigation of heterogeneous deformation of grains via a combination of crystal plasticity finite element method (CPFEM) and CA model (CPFEM-CA). Raabe and Becker (2000) made a creative contribution in this

regard by establishing a coupling method, which was used to simulate microstructure evolution in heterogeneously deformed polycrystalline aluminum. Subsequently, CPFEM-CA was applied to titanium (Wu et al., 2013) and magnesium alloys (Popova et al., 2015, 2016). In addition, a coupled method reported by Li et al. (2016) explained the relationship between the morphological characteristics of dynamic recrystallized grains and heterogeneous deformation by CPFEM and CA. The accuracy of the simulation was verified by isothermal compression tests of the TA15 alloy. Recently, this approach was further improved by Zhang et al. (2020), who modeled the thermal interface grooving and deformation anisotropy of titanium alloys with a lamellar colony by a combination of the Monte Carlo (MC) method and CPFEM. Lately, Nagra et al. (2020) creatively improved the rate-tangent-crystal plasticity-fast Fourier transform framework proposed by Nagra et al. (2017, 2018) to model the DRX behavior of hexagonal closed-packed (HCP) AZ31 alloys and further investigated the formability of the alloys by coupling the M-K approach with the CA method. The improved numerical framework has the advantage of quantifying the intrinsic characteristics, including macro stress, strain, twinning volume fraction, micromechanical fields, texture evolution, and local dislocation density of HCP alloys. Although the abovementioned models can substantially reflect the physical metallurgy principles from macroscale forming to microscale microstructural evolution, they do not consider the variations in the Zeller-Hollomon parameter. Compared with the traditional CA model describing the evolution of dislocation density by the Kocks-Mecking (KM) model (Mecking and Kocks, 1981), CPFEM can accurately demonstrate heterogeneous deformation in a single grain. However, large plastic deformation and inaccuracy of identification parameters may lead to significant challenges in the application of this coupled model in actual metal forming.

Efforts have also been made to develop other hybrid models to meet the practical demands in metal forming. Lee and Im (2010) proposed a new way to describe the DRX of copper during non-isothermal hot compression using the traditional CA method and FE. According to the acquired results, this approach could predict local microstructures during non-isothermal forming. In addition, Takaki et al. (2014) established a novel multiscale hot-working model with DRX, which tracked the microstructure evolution by the multi-phase-field DRX (MPF-DRX) model and synchronized the macroscopic mechanical behavior according to the J2 flow theory. Zhao et al. (2016) innovatively proposed a model for DRX by integrating a fast Fourier transform-based elastic-viscoplastic model with a phase-field recrystallization model. The novelty of this model is that it systematically and simultaneously considers the relationship between the microstructural changes and the mechanical properties of materials during hot plastic deformation. This approach was further improved in a subsequent study by Zhao et al. (2018). These studies offer the possibility of a more realistic simulation of hot working with DRX, specifically for heterogeneous and non-isothermal hot working processes.

This study aims to develop a straightforward and effective method that can be easily combined with commercial FE computer codes to predict microstructure evolution during

actual hot metal forming with dDRX. Furthermore, recent studies on all aspects of the multilevel CA (MCA) model (Chen et al., 2020) have been discussed for further improvement. To the best of our knowledge, this is the first study on the application of multiscale modeling to predict microstructure evolution under real hot-working conditions with dDRX.

The study is organized as follows: the materials used herein, macroscopic extrusion experiment, and microscopic investigations are briefly introduced in Section 2; basic theories of the MCAFE-dDRX model are comprehensively discussed in Section 3; critical results with an emphasis on the evolution of local microstructure during hot extrusion and detailed discussions are presented in Section 4; and conclusions are provided in Section 5.

## **2. Materials and experiment**

Commercially pure copper was used for model calibration and verification. Hot extrusion was conducted to estimate the accuracy of the dDRX prediction for pure copper at different Zener-Hollomon parameters.

To obtain a uniform initial microstructure, the cylindrical billet was vacuum annealed at 390 °C for four hours and then furnace-cooled to room temperature. A test campaign was chosen to acquire high-deformation level characteristics of extrusion. Moreover, owing to the heterogeneous plastic deformation of a billet section, the same billet presented a wide gradient of plastic strain. The experiments were carried out at a combined initial temperature of 300 °C and a speed of 3 mm/s. The billet was heated to the target temperature in a vacuum furnace and then moved to a container. A k-type thermocouple temperature measurement system was employed in the test campaign. Herein, two thermocouples were mounted on the inner surface of the container to efficiently monitor the thermal conditions of the reduced billet section during hot-extrusion.

After the test campaign, the extruded billet was quenched with water and further sliced. Specimens were obtained by cutting the sliced billet parallel to the extrusion axis and were polished with SiC papers and diamond suspensions to fully achieve a mirror surface for further electron-backscattered diffraction (EBSD) investigations at several points. A VEGA 3XMU (LaB6) field emission scanning electron microscope equipped with an Oxford/Nordlys EBSD detector was used to examine the microstructure evolution during dDRX. To obtain a relatively high indexing rate of the EBSD pattern, the specimens were initially mechanically polished with SiC papers having 600, 800, 1200, and 4000 grit sizes, followed by fine polishing with 3, 1, and 0.3 μm diamond suspensions and a 0.05 μm alumina suspension. To eliminate the small deformation and residual stress on the polished surface, vibratory polishing was performed using 0.02 silica suspension for two hours. Measurement campaigns were executed at an acceleration voltage of 15 kV and a working distance of 20 mm. The scanned area and step size were 125 μm × 125 μm and 0.25 μm, respectively. Data were processed by the AZtec system (Oxford Inst.).

## **3. MCAFE-dDRX model**

### 3.1. 3D MCA modeling of dDRX

In the proposed MCAFE-dDRX numerical framework, the idea of multilevel cellular space was incorporated into the traditional CA simulation for ensuring closer to the real deformation process and higher accuracy of grain morphology. Herein, the integrated MCA model consisted of four main sub-modules: (1) physical metallurgical parameter calculation (PMPC) module, which could track the dislocation density, calculate the driving forces, and record the orientations; (2) multilevel recrystallized nucleation (MRN) module, which introduced the concept of effective nucleation into the traditional CA model; (3) recrystallized grain growth (RGG) module, which included the theory of grain growth driven by the dislocation density difference; and (4) full-field grain boundary identification (FGBI) module, which determined whether the cell was located at the grain boundary. Figure 1 shows the basic integration scheme as an example of the application of MCA.

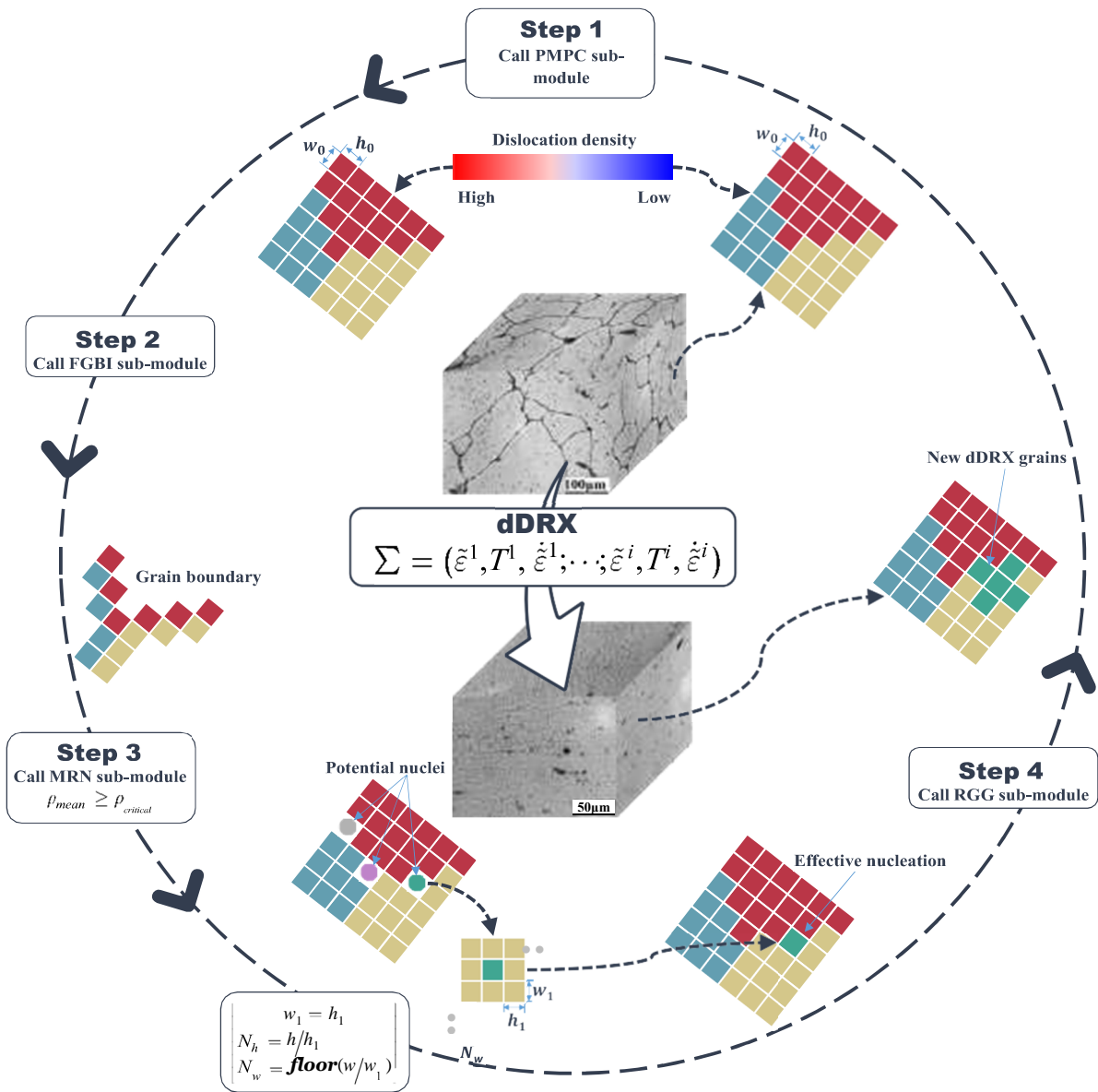


**Fig. 1.** Schematic of the implementation of MCA.

At first, the initial microstructure was described using the regular geometry, such as square lattice for 2D ( $w_0 = h_0$ ) and cube for 3D; then, the PMPC and MRN modules were set up to explain the nucleation and equiaxed growth of newly recrystallized nuclei/grains in the same coordinate system at different levels of cellular space, respectively. Furthermore, theoretical models were described in detail to better understand how to introduce the physical metallurgy principle of dDRX into MCA.

Moreover, to appropriately explain the nucleation and growth of a newly recrystallized grain in dDRX, 2D MCA was further extended to 3D space in this study. In addition, the basic 3D MCA principles in terms of the neighborhood type, boundary conditions, state variables, and cellular state switching rules were comprehensively introduced (see Appendix A1).

### 3.1.1. Modeling of dislocation evolution

The dislocation density  $\rho_i$  in the  $i^{th}$  grain, which was speculated to be uniform in a grain,

$$\rho_i$$

was calculated by the KM model as follows (Mecking and Kocks, 1981):

$$\frac{d\rho_i}{d\tilde{\varepsilon}} = k_1\sqrt{\rho_i} - k_2\rho_i \quad (1)$$

where  $\tilde{\varepsilon}$  is the effective strain,  $k_1$  represents the working hardening, and  $k_2$  is a function of

the Zener-Hollomon parameter that represents the dislocation annihilation due to DRV.

By integrating Eq. (1), the dislocation density was calculated as follows:

$$\rho_i = \left( \frac{k_1}{k_2} - \frac{k_1}{k_2} e^{-\frac{k_2}{2}\tilde{\varepsilon}} + \sqrt{\rho_0} e^{-\frac{k_2}{2}\tilde{\varepsilon}} \right)^2 \quad (2)$$

where  $\rho_0$  can be derived from the Bailey-Hirsch equation:

$$\rho_0 = \left( \frac{\sigma_0}{\alpha\mu b} \right)^2 \quad (3)$$

where  $\sigma_0$  is the initial stress,  $\alpha$  is a dislocation interaction term which is taken as 0.5,  $\mu$  is the shear modulus, and  $b$  is the Burgers vector. In practice,  $\sigma_0$  can be extracted from the true stress-strain curves. In most cases,  $\sigma_0 = \sigma_{0.2\%}$ .

In the MCA simulation, the dislocation densities of all the cells are calculated by Eq. (1) at various forming temperatures and strain rates, and then, the average dislocation density

$\rho_{mean}$  can be obtained as follows:

$$\rho_{mean} = \frac{1}{N_{total}} \sum_i^{N_{total}} \rho_i \quad (4)$$

where  $N_{total}$  is the total number of cells in the MCA model. According to the Bailey-Hirsch

equation, the macro stress can be acquired by  $\sigma = \alpha\mu b\sqrt{\rho_{mean}}$ .

When  $\frac{d\rho}{d\bar{\epsilon}} = 0$ , the saturation dislocation density can be achieved by

$$\rho_{saturation} = \left(\frac{k_1}{k_2}\right)^2 \quad (5)$$

By substituting Eq. (5) into Eq. (4), we obtain

$$\sigma_{work\_hardening} = \sigma_{saturation} + (\sigma_0 - \sigma_{saturation})e^{-\frac{k_2}{2}\bar{\epsilon}} \quad (6)$$

where  $\sigma_{work\_hardening}$  is the flow stress when work hardening plays a dominant role.

Considering that  $\mu$  changes with the deformation temperature, the following equations is acquired.

$$k_1 = \frac{\sigma_{saturation}k_2}{\alpha\mu_0 \left[1 - 0.91 \times \left(\frac{T - 300}{T_m}\right)\right] b} \quad (7)$$

where  $T$  is the deformation temperature, and  $T_m$  is the melting point of the deformed material. The saturated stress is calculated as follows:

$$\sigma_{saturation} = \left[ A_1 \dot{\bar{\epsilon}} \exp\left(\frac{Q_{activation}}{RT}\right) \right]^{1/A_2} \quad (8)$$

### 3.1.2. Modeling of nucleation and growth

To simplify the model, the dislocation density in each recrystallized nucleus returns to the initial value, which is set to  $10^{-10}/m^2$ , when nucleation takes place. Then, the dislocation density evolves differently for the matrix and the newly recrystallized grains. Without loss of generality, the onset of nucleation is associated with the bulging mechanism of grain boundaries owing to the accumulation of dislocations. When the dislocation density of a deformed matrix reaches a critical value called the threshold energy of dDRX, nucleation occurs. The critical dislocation density  $\rho_{critical}$  can be calculated by (Robers and Ahlblom, 1978)

$$\rho_{critical} = \left(\frac{20\gamma_{\beta}\dot{\bar{\epsilon}}}{3bIM\tau^2}\right)^{1/3} \quad (9)$$

where  $\gamma_\beta$  is the grain boundary energy per unit area;  $l$  is the average mean free path of the mobile dislocation, which can be calculated by  $l = 20 \sqrt{\rho_0}$  (Takaki et al., 2014);  $M$  is the grain boundary mobility, and  $\tau$  is the dislocation line energy, which is expressed by

$$\tau = \mu \frac{b^2}{2} \rho_{critical}$$

$\gamma_\beta$  is calculated by the Ready-Shockley equation:

$$\gamma_\beta = \begin{cases} \gamma_m & \theta_\beta \geq 15^\circ \\ \gamma_\beta = \gamma_m \frac{\theta_\beta}{\theta_m} \left[ 1 - \ln \left( \frac{\theta_\beta}{\theta_m} \right) \right] & \theta_\beta < 15^\circ \end{cases} \quad (10)$$

where  $\theta_\beta$  is the misorientation between the  $i^{th}$  cell and its neighboring cells. The values of  $\beta$  range from 1 to 6 as the total number of neighboring cells for 3D MCA is 6. The detailed method to calculate  $\theta_\beta$  presented in Appendix A3. The energy for HAGBs can be directly calculated as follows (Chen et al., 2009):

$$\gamma_m = \frac{\mu b \theta_m}{4\pi(1-\nu)} \quad (11)$$

where  $\gamma_m$  and  $\theta_m$  are the boundary energy and the misorientation for HAGBs, respectively, and  $\nu$  is Poisson's ratio.

The nucleation rate per unit grain boundary area for dDRX is calculated as

$$\dot{n}_{dDRX} = C_{dDRX} \dot{\epsilon} \exp\left(-\frac{Q_{activation}}{RT}\right) \quad (12)$$

where  $C_{dDRX}$  is a constant, which can be determined by an inverse analysis method (Jin and Cui, 2010; Chen et al., 2020) and can also be calculated by an experimental measurement method for a specific deformation condition;  $Q_{activation}$  is the activation energy; and  $R$  is the universal gas constant.

The energy difference in terms of dislocation density between the recrystallized grains and the matrix supplies the thermodynamic driving force for the growth of nuclei.

Considering the solution drag effect, the equiaxed growth velocity of nuclei/grains can be expressed as

$$v_\beta = \psi M F_\beta = \left[ D_\psi \dot{\epsilon}^{n_\psi} \exp\left(-\frac{Q_\psi}{RT}\right) \right] \left[ \frac{\delta D_{ob} b}{KT} \exp\left(-\frac{Q_b}{RT}\right) \right] \left[ \tau(\rho_{matrix} - \rho_i) - \frac{2\gamma_\beta}{r_i} \right] \quad (13)$$

where  $\psi$  represents the solution drag effect;  $F_\beta$  is the driving force;  $D_\psi$ ,  $n_\psi$  and  $Q_\psi$  are material constants;  $\delta$  is the characteristic grain boundary thickness;  $D_{ob}$  is the boundary self-diffusion coefficient;  $Q_b$  is the grain boundary diffusion activation energy;  $K$  is the

Boltzmann constant;  $\rho_{matrix}$  is the dislocation density of the matrix;  $\rho_i$  is the dislocation density of the  $i^{th}$  cell; and  $r_i$  is the equivalent average radius of a recrystallized grain, which is expressed by

$$r_i = \left( \frac{3N_i V_{cel}}{4\pi} \right)^{1/3} \quad (14)$$

where  $N_i$  is the total number of cells belonging to a recrystallized grain, and  $V_{cel}$  is the volume of each cell.

In MCA simulation, the time step  $\Delta t$  is defined as the ratio of the cell diameter and to the maximum grain boundary velocity  $v_{max}$ , which is calculated by

$$\Delta t = \frac{d_0}{v_{max}} = \frac{k_2^2 d_0}{M \tau k_1^2} \quad (15)$$

where  $d_0$  is evaluated using Eq. (14) when  $N_i = 1$ .

Then, the strain increment is expressed as  $\Delta \varepsilon = \dot{\varepsilon} \Delta t$ . The grain boundary migration distance at time  $t$  is calculated as  $l_\beta^t = l_\beta^{t-\Delta t} + v_\beta \Delta t$ .

### 3.2. FE modeling

In this study, a simulation campaign was conducted using the commercial software FORGE developed based on a rigid-viscoplastic thermo-mechanical FE formulation. Figure 2 shows meshed FE models for the initial billet and dies.

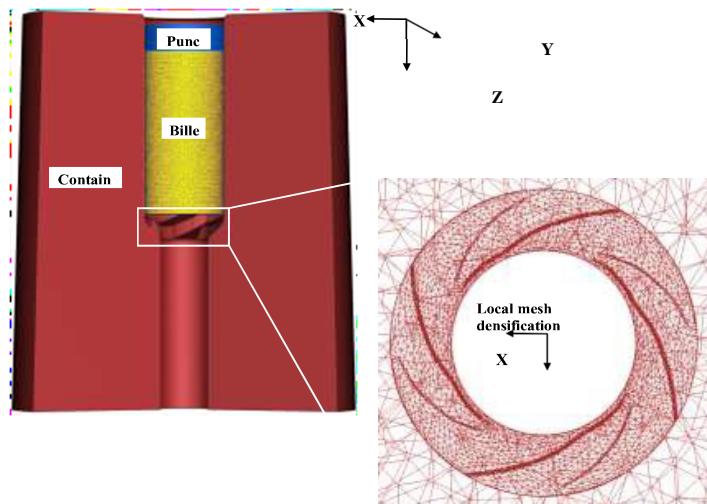


**Fig. 2.** Schematic of meshed finite element models.

The entire billet was analyzed based on the geometrical characteristics of the container entrance. A 10-node tetrahedron element was used in the meshed billet. A refinement window was employed to achieve a higher mesh density around the container entrance region

than those in other regions. The mesh density ratio between the region inside and outside the window was specified as 10. The total number of elements for the billet was 336,000. This number was kept constant to ensure proper element size. The numbers of tetrahedron elements employed for the punch and container were 93,438 and 180,628, respectively. The container and punch were considered perfectly rigid, whereas the copper bar billet was regarded as rigid-plastic. The elements for the two dies were only used to calculate the temperature fields. During the FE simulation, the copper bar billet was remeshed when the mesh was distorted in terms of zero/negative Jacobian. The data acquired using the old mesh were automatically interpolated to the new mesh, and then, the FE simulation was continued. The boundary conditions in the FE simulation and thermophysical properties of the deformed billet were as follows: (1) The friction condition with oil lubricant was used, and the friction coefficient of 0.15 was employed; (2) Radius and height of the initial billet: 30 and 40 mm, respectively, and extrusion ratio: 1.6; (3) Speed of the punch: 3 mm/s; (4) Environment temperature: room temperature, and temperature of the billet: 300 °C; (5) Heat transfer coefficient between the billet and the dies: 5 N/s/mm/°C; (6) Convection coefficient to the environment: 0.02 N/s/mm/°C; and (7) Tabular data format was used to represent the flow behavior of the studied pure copper, which is widely used and recommended for FORGE.

### *3.3. Integration scheme of the MCALE-dDRX model*

Figure 3 depicts the flowchart of the current numerical simulation procedure. The integrated modeling approach mainly includes the following two parts: a plastic deformation FE model and MCA. Macroscopic physical fields, such as temperature, strain, and strain-rate fields, of the dispersed element nodes, were calculated by FE simulation. Herein, element nodes were recognized as the material points of the billet. After tracking the thermal and deformation histories of the element nodes, the MCA model was employed to predict the microstructure evolution during the entire hot deformation history for each element node. The macroscopic physical fields were used as the input data in MCA (See Appendix B). Finally, the macroscopic physical fields were obtained by FE calculation, and the size and morphology of the recrystallized grains and recrystallization volume fraction of element nodes changed with deformation. According to the distribution of data, the global microstructural information of the deformed billet and the local microstructure represented by element nodes were also quantified by MCA.

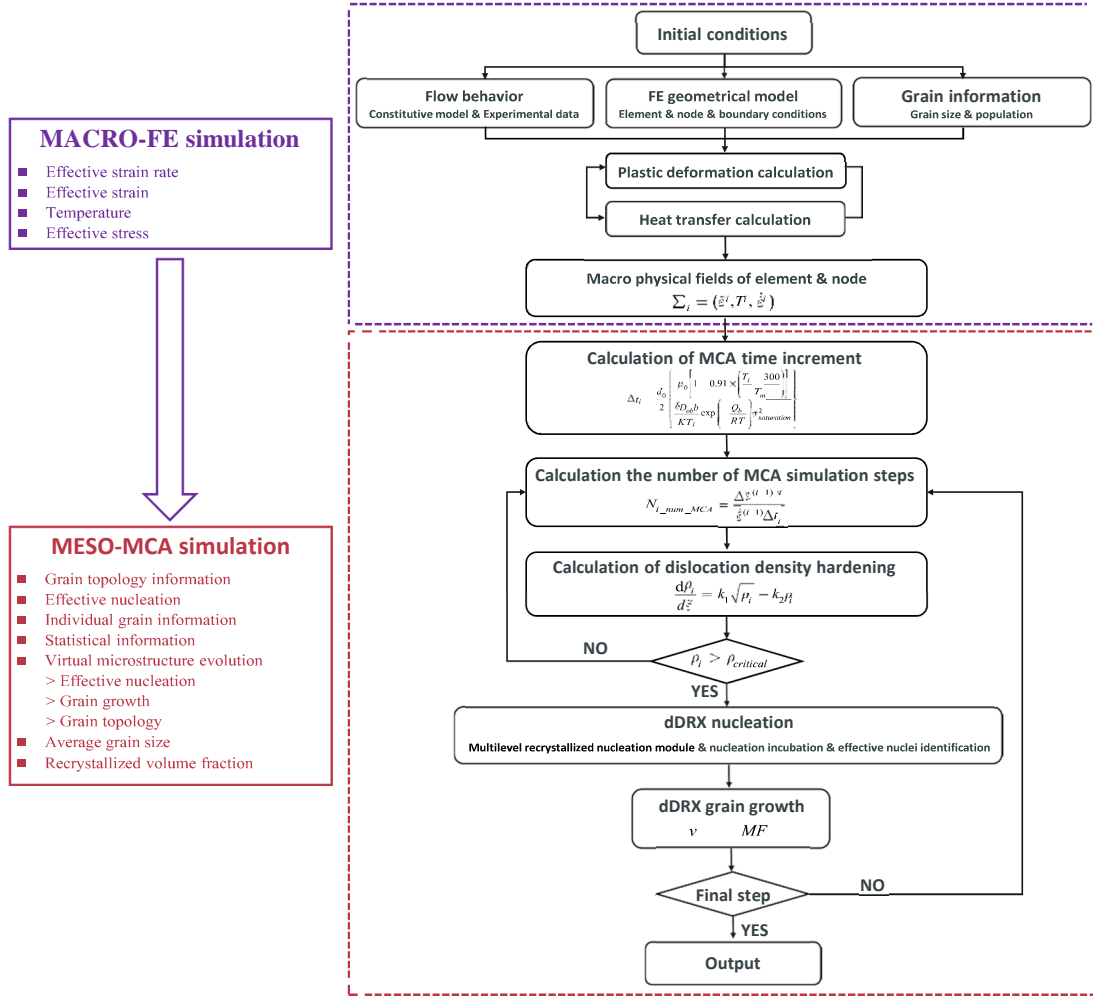


**Fig. 3.** Flowchart of the multiscale modeling method.

## 4. Results and discussion

### 4.1. Verification of the 3D MCA model

To verify the 3D MCA model, initially, simulations were conducted, and then, the simulation results were compared with the findings of the classical experimental study on the dDRX behavior of pure copper under isothermal hot compression reported by Blaz et al. (1983). Material parameters employed in the present simulations and their physical meanings are provided in Table 1.

**Table 1**

Material constants for pure copper (Ding and Guo, 2001).

Symbol	Physical meaning	Value
$\mu_0$	Shear modulus (MN/m <sup>2</sup> )	$4.21 \times 10^4$
$Q_{activation}$	Activation energy for dDRX (kJ/mol)	261
$Q_b$	Boundary diffusion activation energy (kJ/mol)	104
$\delta D_{ob}$	Boundary self-diffusion coefficient (m <sup>3</sup> /s)	$5.0 \times 10^{-15}$
$Q_b$	Grain boundary diffusion activation energy (kJ/mol)	104

$T_m$	Melting temperature (K)	1356
$K$	Boltzmann's constant (J/K)	$1.38 \times 10^{-23}$
$b$	Burgers vector (m)	$2.56 \times 10^{-10}$
$R$	Ideal gas constant (J/mol)	8.314
$D_\psi$		$1.72 \times 10^4$
$n_\psi$	Material constants for solution drag effect	0.29
		$7.60 \times 10^4$
$Q_\psi$		

#### 4.1.1 Features of the flow stress curves

Flow stress links the flow behavior with microstructure evolution. It is commonly believed that predicting the flow stress in hot working is highly fundamental to understanding the plastic flow behavior of materials. Moreover, the typical characteristics of the flow stress curves of dDRX correspond to the microstructure evolution and mechanical behaviors of materials. Therefore, the intrinsic characteristics of the measured flow curves were systematically investigated.

Stress-strain curves were predicted by MCA under a wide range of deformation conditions and were compared with the experimental data shown in Fig. 4. Generally, the simulated results suitably agree with the experimental data. However, a slight discrepancy is evident during the work-hardening stage. This is caused by the limitation of the current KM dislocation density model (Mecking and Kocks, 1981) in determining the flow stress of the material during the initial stage of hot compression in the MCA simulation. Nevertheless, the simplicity of the dislocation density model appropriately balances the calculation precision and efficiency accordingly. Furthermore, note that the oscillation of flow stress occurs at a

small Zener-Hollomon parameter  $\dot{\epsilon} \exp\left(\frac{Q_{activation}}{RT}\right)$  (for example, 875K, 975K and 1075K) at the strain rate of  $2 \times 10^{-3} \text{s}^{-1}$  and initial grain size of  $78 \mu\text{m}$ . This phenomenon has also been examined by both theoretical and experimental studies (Jonas et al., 2009).

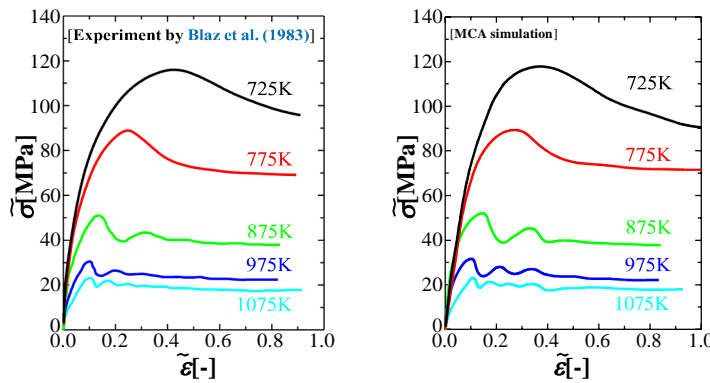


**Fig. 4.** Comparison between the flow stress curves obtained by MCA simulation at different temperatures and a strain rate of  $2 \times 10^{-3} \text{s}^{-1}$ , and the experimental data reported by Blaz et al. (1983) using the initial grain size of  $78 \mu\text{m}$  for both simulation and experiment.

Shape characteristics of true stress-strain curves significantly depend on the relationship between the threshold for the initiation of dDRX ( $\tilde{\epsilon}_{critical}$ ) and the strain required for the completion of one cycle of recrystallization ( $\tilde{\epsilon}_{cycle}$ ); if  $\tilde{\epsilon}_{critical} > \tilde{\epsilon}_{cycle}$ , complete recrystallization occurs before the critical strain in the newly recrystallized grains is achieved, and the flow stress is characterized by multippeak oscillations. In contrast,  $\tilde{\epsilon}_{cycle} > \tilde{\epsilon}_{critical}$  indicates that a subsequent recrystallization cycle is again initiated in the newly recrystallized grains in which the previous cycle has not been completed, and finally, the flow stress curve shows only one peak and no oscillation. Moreover, the oscillation may be more easily observed in the flow stress curve at high temperatures or low strain rates (that is, at small Zener-Hollomon parameters).

To better analyze the oscillation in the true stress-strain curves, the values of  $\tilde{\epsilon}_{critical}$  determined by Eq. (9), and  $\tilde{\epsilon}_{cycle}$  predicted by MCA according to the Zener-Hollomon parameters are presented and compared in Table 2.

**Table 2**

Critical material parameters for pure copper at various Zener-Hollomon parameters.

Zener-Hollomon[-]	$\rho_{critical}$ [ $10^{12}m^{-2}$ ]	$\tilde{\epsilon}_{critical}$	$\tilde{\epsilon}_{peak}$	$\tilde{\epsilon}_{cycle}$	$\tilde{\epsilon}_{critical}/\tilde{\epsilon}_{cycle}$	$\tilde{\epsilon}_{critical}/\tilde{\epsilon}_{peak}$
$1.28 \times 10^{16}$	210.24	0.113	0.42	1.017	0.11	0.27
$7.82 \times 10^{14}$	108.44	0.073	0.25	0.607	0.12	0.29
$7.63 \times 10^{12}$	31.69	0.039	0.14	0.185	0.21	0.28
$1.92 \times 10^{11}$	12.35	0.030	0.11	0.128	0.23	0.27
$9.63 \times 10^9$	3.68	0.025	0.098	0.082	0.30	0.26

$\tilde{\epsilon}_{cycle}$  is generally larger than  $\tilde{\epsilon}_{critical}$  in the Zener-Hollomon range. It is hypothesized that the relationship between  $\tilde{\epsilon}_{critical}$  and  $\tilde{\epsilon}_{cycle}$  may not be the only reason for the oscillation of flow stress. However, note that  $\tilde{\epsilon}_{critical}/\tilde{\epsilon}_{cycle} > 0.2$  always results in oscillation. As reviewed

by Huang and Logé (2016), oscillation primarily depends on the combined effects of the accumulation rate of dislocations in newly recrystallized grains and the grain boundary volume of the matrix. Thermomechanical processing parameters, such as temperature and strain rate, play a dominant role in the accumulation of dislocations in newly recrystallized grains. The grain boundary volume of the matrix is substantially influenced by the initial grain size of the matrix (Blaz et al., 1983; Sakai et al., 2014). The combined effects of these two factors govern the accumulation rate of dislocations during hot working and eventually control the shape characteristics of the true stress-strain curves.

To reveal the correlation between the grain boundary volume fraction and oscillation, the relationships between the initial matrix grain size, the evolution of the grain boundary area, and the true stress-strain curve were investigated. Figure 5 depicts the effects of the initial

grain boundary volume fraction on the flow stress curves and the mean grain size at the strain rate of  $2 \times 10^{-3} \text{s}^{-1}$  and temperature of 725 K.

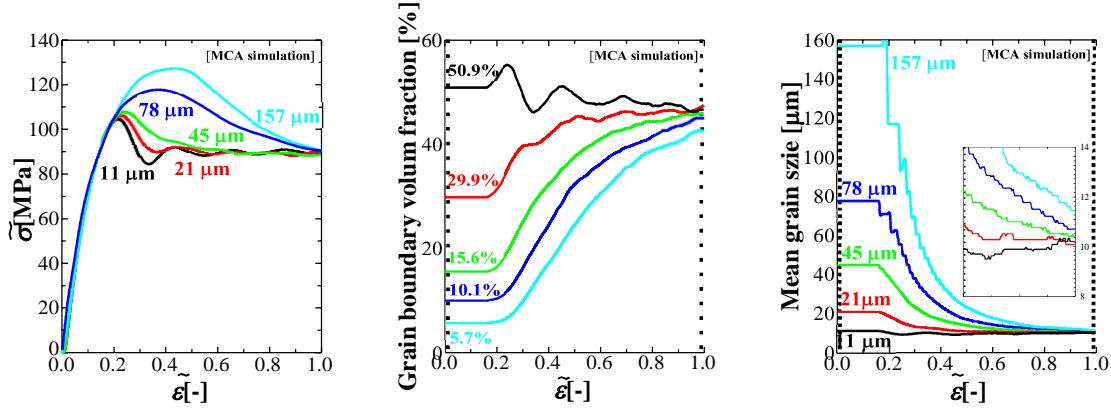


**Fig. 5.** Evolution of the grain boundary volume fraction, flow stress curves, and mean grain size with different sizes of the initial matrix at a temperature of 725 K and a strain rate of  $2 \times 10^{-3} \text{s}^{-1}$  determined by MCA simulation. The initial grain boundary volume fractions were 5.7%, 10.1%, 15.6%, 29.9% and 50.9%, corresponding to the initial grain sizes of 157, 78, 45, 21, and 11  $\mu\text{m}$ , respectively.

According to the experimental data, the steady grain size  $d_{srex}$  eventually reaches 9.8  $\mu\text{m}$  (Blaz et al., 1983), and the predicted value is 10.7  $\mu\text{m}$ . As can be noticed in Fig. 5, flow stress oscillates when  $d_0$  is decreased to 21  $\mu\text{m}$  ( $d_0 < 2d_{srex}$ ), which corresponds to the initial

grain boundary volume fraction of 50.9%. Oscillation considerably increases with a further decrease in  $d_0$  to 11  $\mu\text{m}$ . The simulated results of the influence of grain boundary volume of the matrix on flow stress appropriately agree with the common empirical criterion proposed by Sakai et al. (2014) and the numerical simulation results reported by Ding and Guo (2001): if  $d_0 < 2d_{srex}$ , adequate quantities of grain boundaries are provided for the nucleation of

dDRX in the matrix, and the growth of the newly recrystallized grains (also termed the migration of LAGBs) proceeds effectively and continuously. The nearly synchronous recrystallization finally leads to the oscillation of flow stress with multiple peaks.

Nevertheless, if  $d_0 > 2d_{srex}$ , the increase in  $d_0$  (indicating a decrease in the grain boundary

volume) commonly results in the lack of grain boundaries for the nucleation of the next cycle of dDRX. Under this condition, recrystallization progresses asynchronously, and the flow stress curves have only one peak with no oscillation.

Another interesting finding of this simulation is that the steady-state average grain size is almost independent of the initial grain size (initial grain boundary volume fraction), whereas the recrystallization kinetics and the flow stress curve significantly depend on the initial grain size (Fig. 5). A potential reason for this is that smaller initial grain size provides sufficient grain boundary cells as potential nucleation sites. Furthermore, recrystallization can be promoted by a fine-grain matrix because the newly recrystallized grains may impinge earlier to achieve a certain grain boundary migration rate (Yazdipour et al., 2008; Chen and Cui,

2012). In contrast, the lowest initial grain boundary volume fraction of 5.7% leads to a noticeably coarser mean grain size of 11.5  $\mu\text{m}$ . Note that with an increase in the volume fraction, the steady-state is not realized in the simulated strain range.

Based on the abovementioned simulation and analysis, the classifications  $\tilde{\epsilon}_{critical} > \tilde{\epsilon}_{cycle}$  and  $\tilde{\epsilon}_{critical} < \tilde{\epsilon}_{cycle}$  were slightly oversimplified to determine the occurrence of oscillation, mainly because  $\tilde{\epsilon}_{cycle}$  was substantially dependent on the average grain size, which varied when dDRX continuously proceeded. Although the empirical criterion proposed by Sakai et al. (2014) reflects the effective nucleation mechanism to a certain extent (Peczak and Luton, 1993, 1994), in reality, it is difficult to obtain the steady grain size  $d_{srex}$  without performing experiments.

Many other theories aim to explain more specific metallurgical mechanisms of oscillation in flow stress curves. For example, dislocation density has been divided into two parts: homogenous dislocation density stored in the subgrain walls and dislocation density in the interior of the subgrains. The subgrain interior dislocation density provides the driving force for the grain boundary migration, indicating that the accumulation and annihilation rates of this dislocation density govern the shape characteristics of the flow stress curve (Ding and Guo 2001). Thus, designing microscopic experiments to separately quantify the effects of these two types of dislocation densities on the flow stress curve would be of considerable interest.

#### 4.1.2 Influence of temperature on the recrystallization kinetics

Recrystallization kinetics presents a phenomenological description of the degree of dDRX. To study the influence of temperature on the recrystallization kinetics, the simulated recrystallized volume fractions under a wide range of deformation conditions are plotted in Fig. 6. The simulated data were compared with the theoretical results by converting them to the Johnson-Mehl-Avrami-Kolmogorov (JMAK) plot (Rollett, 2004) using the following equation:

$$V = 1 - \exp(-Bt^m) \quad (16)$$

where  $V$  is the recrystallized volume fraction, and  $B$  and  $n$  are material constants providing information about the dDRX nucleation rate and growth. At a constant strain rate  $\dot{\epsilon}$ , the time  $t$  in Eq. (16) can be calculated by  $t = (\tilde{\epsilon} - \tilde{\epsilon}_{critical}) / \dot{\epsilon}$ . The fitting results of straight lines imply that the slopes of  $m$  range from 1.3 to 1.5, which are consistent with the values of  $m$  for pure copper undergoing dDRX (Goetz and Seetharaman, 1998; García et al., 2000; Zhao et al., 2016, 2018).

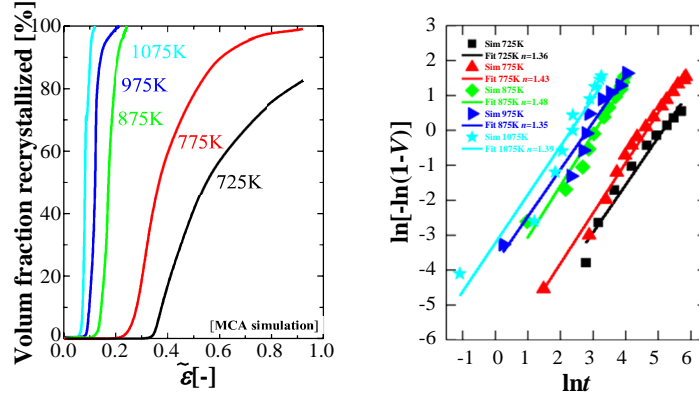


**Fig. 6.** Evolution of the average grain size at different temperatures and a strain rate of  $2 \cdot 10^{-3} \text{ s}^{-1}$  predicted by MCA simulation. Comparison between the average grain sizes obtained by simulation and experiment using an initial grain size of  $78 \text{ }\mu\text{m}$ .

In addition, the relationship between  $\tilde{\varepsilon}_{critical}$  and  $\tilde{\varepsilon}_{peak}$  is of significant practical importance

(Poliak and Jonas, 2003; Huang and Logé, 2016). Therefore, the values of  $\tilde{\varepsilon}_{critical}/\tilde{\varepsilon}_{peak}$  during dDRX in the tested Zener-Hollomon range are also summarized in Table 2. The simulated values of  $\tilde{\varepsilon}_{critical}/\tilde{\varepsilon}_{peak}$  are very close to those reported by Zhao et al. (2016, 2018); however, they are smaller than the  $\tilde{\varepsilon}_{critical} : \tilde{\varepsilon}_{peak}$  ratio according to the experimental observations (Manonukul and Dunne, 1999), which suggests that the very first recrystallization cycle occurs when the critical strain is typically between 0.65 and 0.85 peak strain. As comprehensively explained by Zhao et al. (2018), owing to the limitations of the statistical observation of recrystallization nuclei in terms of bulging mechanism (McQueen, 2004) and transition band mechanism (Sakai et al., 2014), the critical strain of dDRX determined by the metallographic identification of a random 2D cross-section is always larger than the actual strain corresponding to the initiation of dDRX nucleation.

#### 4.1.3 Nucleation and growth features during dDRX

Conventional dDRX has clear nucleation and growth stages. To obtain more detailed information about the nucleation and growth features during dDRX, the evolution of the newly recrystallized grains (except for those acquired after the first round of dDRX) was analyzed (Fig. 7). Generally, the stored energy due to dislocations plays a key role in the driving force of both nucleation and grain growth. As reported by Ghazi et al. (2018) and Wang et al. (2020), grain boundary bulging is one of the typical nucleation mechanisms in pure metals, in which effective nucleation of dDRX is speculated to occur when a subgrain reaches a critical value:

$$r_{critical} = \frac{4\gamma_{\beta}}{\mu b^2 \rho_{critical}} \quad (17)$$

where  $r_{critical}$  is the critical radius of the subgrain. This means that the difference between the

stored energies of the growing subgrain and the deformed matrix is sufficiently high to overcome the capillary force of subgrain. By combining Eqs. (9) and (17), the following critical radius expression is achieved for the subgrain  $i$ :

$$r_{critical} = 2 \left( \frac{3bIM\gamma_{\beta}^2}{20T\dot{\epsilon}} \right)^{1/3} \quad (18)$$

According to Eq. (18),  $r_{critical}$  for triggering effective dDRX nucleation was obtained at a temperature of 875 K and a strain rate of  $2 \times 10^{-3} \text{ s}^{-1}$  with a change in the misorientation between the  $i^{th}$  grain and its neighboring matrix. For example, when the subgrain misorientation was in the range of 1-2° (LAGBs), the critical size of the subgrain was found to be in the range of 0.604-0.835  $\mu\text{m}$ . As demonstrated by Kassner and Barrabes (2005), the critical subgrain size typically ranges from one-tenth to one percent of the initial diameter. Additionally, Zurob et al. (2006) have mentioned that once the size of the subgrain exceeds the critical size, rapid growth of the subgrain takes place. As shown in Fig. 7, the strain near the 0.112 (corresponding to the subgrain size of 0.612  $\mu\text{m}$ ) grain rapidly increases. In addition to nucleation at the matrix, recrystallized grain boundaries are potential sites for dDRX nucleation.

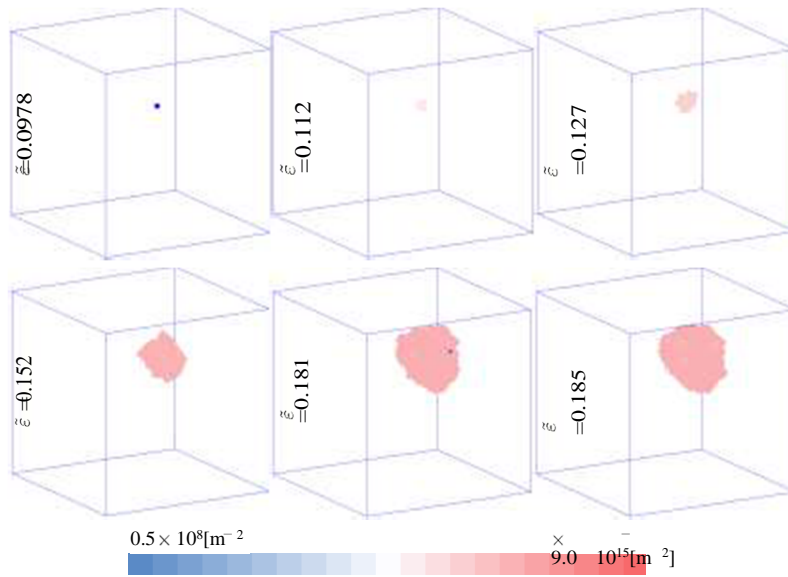


**Fig. 7.** Nucleation and growth of the newly recrystallized grains at different strains and a strain rate of  $2 \times 10^{-3} \text{ s}^{-1}$  and a temperature of 875 K predicted by MCA simulation. Here the blue color represents the nucleus of dDRX with the initial dislocation density of  $10^{10} \text{ m}^{-2}$ . Moreover, the color bar represents the change in the dislocation density of recrystallized grains with an increase in the deformation strain.

Furthermore, a new round of dDRX occurred at previously recrystallized grain boundaries when the strain reached 0.152. Under this strain condition, the dislocation density of the growing dDRX grain was  $4.503 \times 10^{13} \text{ m}^{-2}$ , which was higher than  $\rho_{critical}$  ( $3.169 \times 10^{13} \text{ m}^{-2}$ )

under the simulated Zener-Hollomon condition. Another interesting finding is that not all subsequent nuclei would have an equal opportunity to grow and eventually reach the steady-state grain size. In our simulation, the possible reason for this difference was attributed to the inherent characteristics, namely, the probability of the CA method. Thus, further in-situ observations with specially designed transmission electron microscopy (TEM) are required to effectively reveal the physical metallurgical mechanisms.

#### 4.2. Application and verification of the coupled model

##### 4.2.1. Macroscopic physical field determination by FE simulation

Based on the spiral structure of the container entrance, the entire billet was simulated. More details on the numerical implementation can be found in the literature (Calamaz et al., 2008; Chen et al., 2013). Figure 8 depicts the effective strain and temperature fields over a cross-section of the deformed billet.

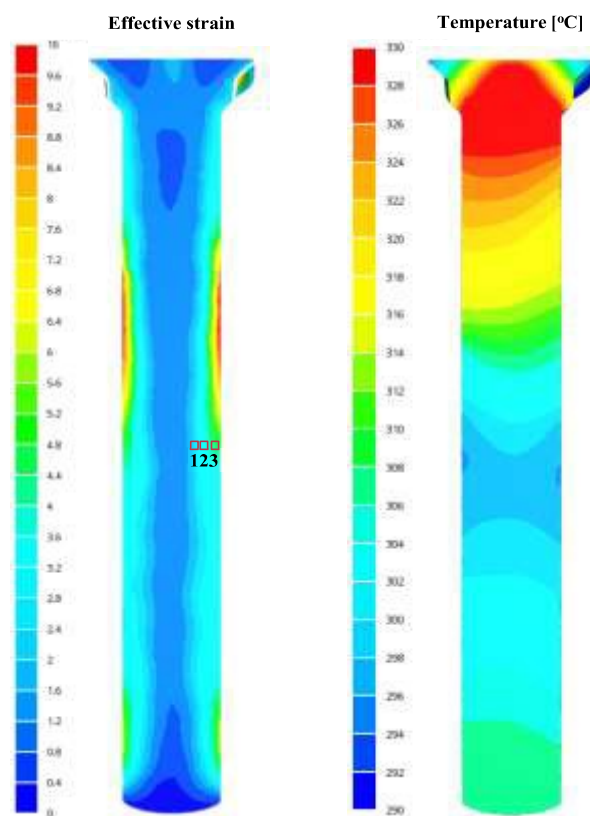


**Fig. 8.** FE simulation of the temperature and strain of the deformed billet. Areas marked by the red boxes with numbers ranging from 1 to 3 in the effective strain distribution figure represent the material points for the following MCA simulation. Characterization positions from right to left are 0.25, 1, and 3 mm from the billet surface.

Geometrical characteristics of the container result in a heterogeneous strain distribution. Moreover, serve plastic deformation increases the temperature of the billet because of the conversion of plastic work into heat. Heat transfer between the billet and the dies and the temperature gradient of the billet were evaluated, as shown in Fig. 8. The obtained results were in good agreement with the FE (Shahbaz et al., 2011) and experimental (Shahbaz et al.,

2016) results calculated using a similar extrusion method, that is, vortex extrusion. To track the history of hot working and demonstrate the inhomogeneous deformation of the billet, three boxed areas are numbered in Fig. 8. These boxed areas represent the material points of the deformed billet, which will be simulated by the MCA model. The qualitative characteristics of these areas are as follows: 3 is close to the deformed billet surface where the material is subjected to a large deformation; 2 represents moderate deformation; and 1 is located a quarter away from the surface of the deformed billet.

To comprehensively investigate the macroscale physical fields, the effective strain  $\tilde{\epsilon}$ , strain rate  $\dot{\epsilon}$ , and temperature  $T$  data were extracted from the element nodes located at the three areas, as shown in Fig. 9. During extrusion, deformation takes place in a nearly enclosed environment, and finally,  $T$  increases due to the transformation of the plastic work into heat. Additionally, heterogeneous deformation leads to strain gradient and non-uniform distribution of  $\tilde{\epsilon}$ . These data simulated by FE calculations were employed as an input in the following MCA simulation.

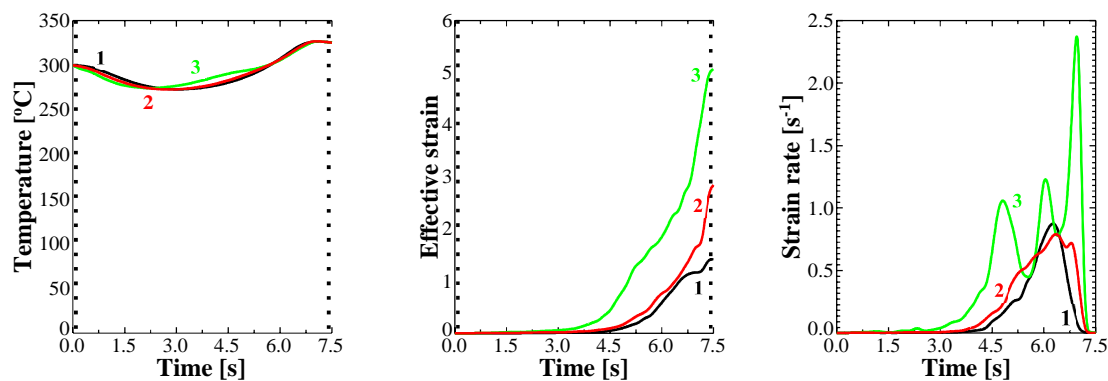


**Fig. 9.** FE calculation of the temperature, effective strain, and strain rate of the investigated element nodes of the deformed billet. The numbers from 1 to 3 represent the material points for the following MCA simulation.

#### 4.2.2. Mesoscopic microstructural features of dDRX

The microstructures at point 1 predicted by the coupled FE and MCA method are shown in Fig. 10, which provides the full-field microstructural information during dDRX. As an example, Fig. 10 presents two ways to illustrate the microstructure evolution during dDRX with an increase in the strain at point 1 by MCA. As shown in Fig. 10, similar to optical images, the cross-sectional view of the simulated microstructure shows the recrystallized grains, the matrix, and the grain boundaries. Herein, one way demonstrates the necklace formation during dDRX due to the occurrence of nucleation only at grain boundary cells. The other way exhibits only the recrystallized grains in the 3D space, which provides an insight into the full-field recrystallized grains.

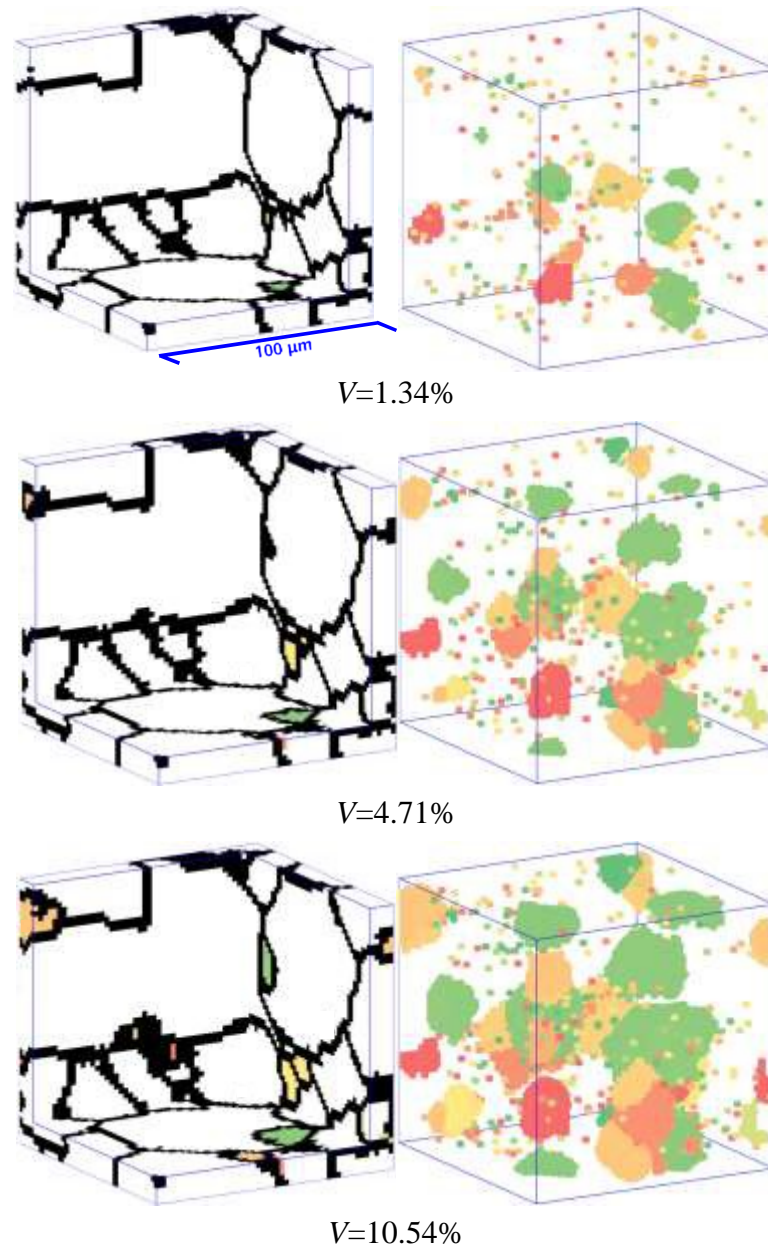


**Fig. 10.** Evolution of recrystallized grains under different strains at point 1 analyzed by MCA simulation using an initial grain size of  $60\ \mu\text{m}$ . The left side of the figure represents the cross-sectional view of the simulated microstructure with a residual thickness of  $10\ \mu\text{m}$ . Here, the white color represents the matrix without dDRX, and the black color represents the grain boundaries. The right side of the figure shows only the recrystallized grains. Here these colors present the orientations of the recrystallized grains.

Figure 11 shows the microstructure and recrystallized fraction during dDRX simulated by the developed 3D MCA model. Complete recrystallization occurred only at point 3, and the average grain sizes at the three points were approximately around  $22.8$ ,  $13.9$  and  $8.6\ \mu\text{m}$ . Although the strain was higher than  $1.2$  at point 1, only partial recrystallization was observed at this point.

The simulated mean grain size significantly decreased in all three cases shown in Fig. 11. A similar phenomenon was also observed in an excellent modeling study of dDRX that is

explained in detail by Zhao et al. (2018). This phenomenon is mainly attributed to the artificial hypothesis of periodic nucleation of new dDRX grains in MCA simulation.

As is commonly known, the Avrami equation can be used to describe the recrystallization kinetics (Rollett, 2004; Jonas et al., 2009; Zhao et al., 2018). According to Eq. (16), the Avrami exponent is presented by  $m = \frac{\partial \ln[-\ln(1-V)]}{\partial \ln t}$ . As shown in Fig. 11, the

recrystallized volume fraction increases following S-type, which has been widely reported previously (Busso, 1998; Janssens, 2003; Jonas et al., 2011; Huang et al., 2018). Based on the simulated data, the Avrami exponents for different deformation conditions are depicted in Fig. 11. The fitting values of  $m$  are between 1.3 and 1.9, which are partly supported by experimental results reported by García et al. (2000).

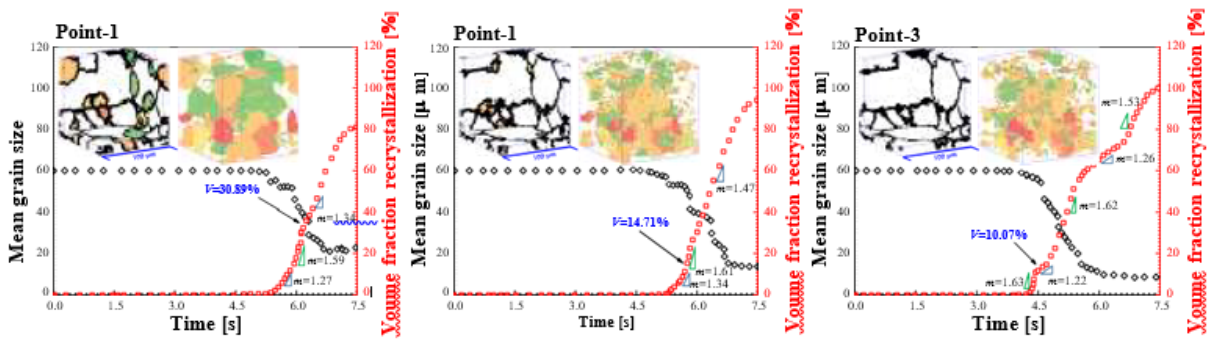


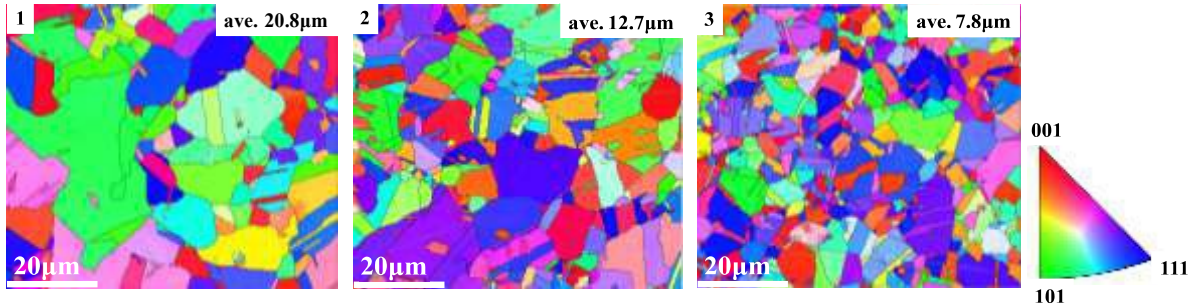
**Fig. 11.** dDRX kinetic curves, mean grain size evolution and grain topology predicted by FE-MCA.

To study the effects of strain rate on recrystallization kinetics, the Avrami exponents were calculated for the clear turning points on the strain rate curves shown in Fig. 11. A higher strain rate may inhibit the increase in the recrystallized volume fraction, which is ascribed to the availability of less time for the growth of newly recrystallized nuclei (Nicolay et al., 2019). Interestingly, according to the simulations, the inhibitory effect of strain rate rapidly attenuates, as shown in Fig. 11. The most probable mechanism for this phenomenon is as follows: as the nucleation rate substantially depends on the strain rate, which has been evaluated in our simulation using Eq. (12), the higher strain rate leads to insufficient time for the growth of the newly recrystallized nuclei and finally for the formation of HAGBs. Nevertheless, these nuclei may continuously grow to compensate for the increase in the recrystallized volume fraction during subsequent strain accumulation.

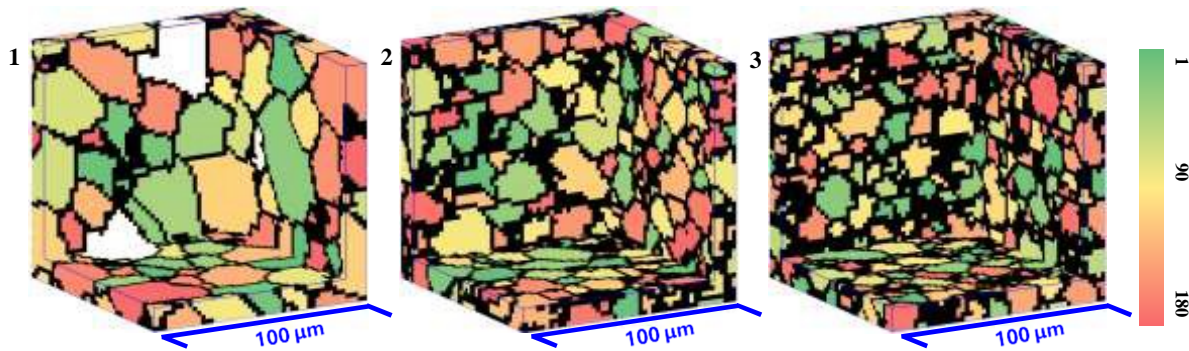
#### 4.2.3. Comparison between the experimental and numerical results

Figure 12 depicts the corresponding microstructures at the three material points after extrusion. Accordingly, the simulated results are shown in Fig. 13. As shown in these figures, due to the individual differences in hot deformation history, the final microstructures of the deformed billet were not relatively uniform. Figure 14 shows a comparison between the simulated and experimental grain radius distributions. The simulated results suitably agree with the experimental results; however, the simulated steady-state grain size is slightly larger than the experimental value. The primary reason for this overestimation may be that the

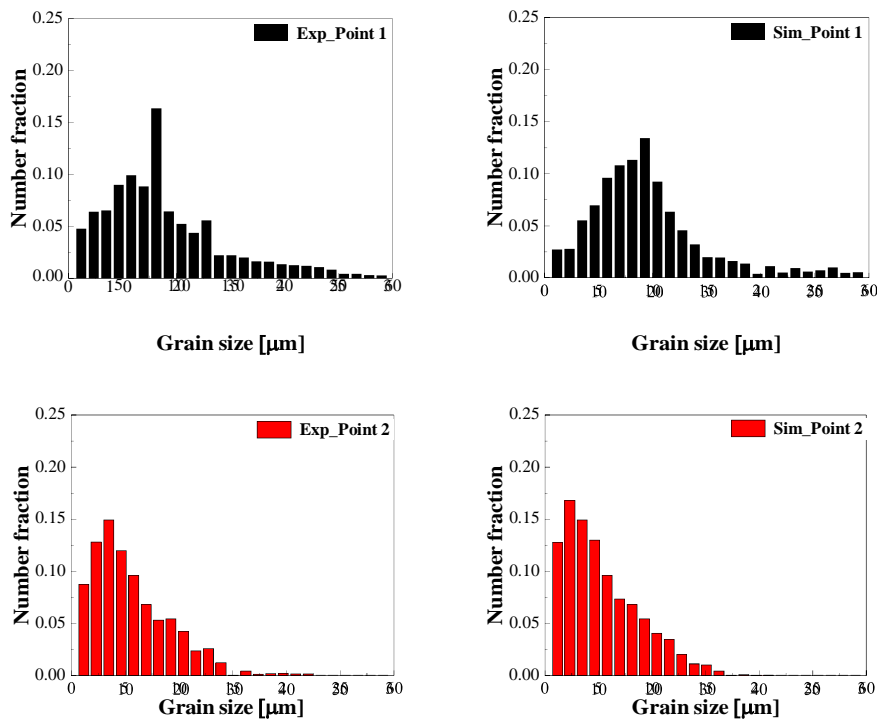
random nucleation mechanism does not consider all possible nucleation sites (for example, dislocation tangles and subgrain walls) in practice (Ding and Guo, 2001). Additionally, the preferential nucleation and growth because of the heterogeneous deformation in the matrix (Sakai et al., 2014; Huang and Logé, 2016) were ignored in the present simulation. This should be a key consideration in future work.



**Fig. 12.** Microstructures at points 1, 2, and 3 by FCE.



**Fig. 13.** Microstructures at points 1, 2, and 3 predicted by MCAFE-dDRX simulation.



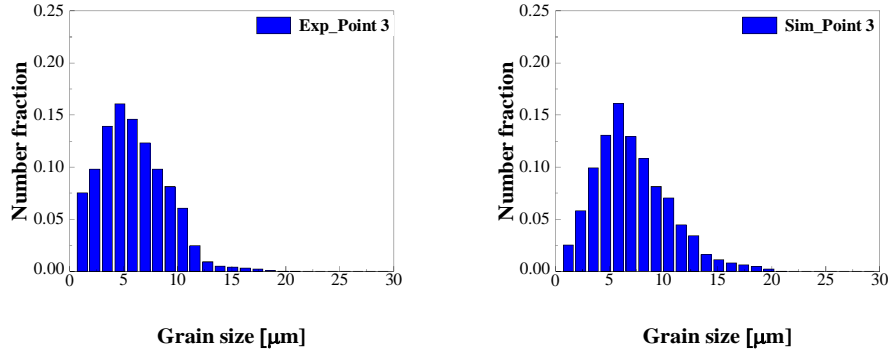


**Fig. 14.** Comparisons between the grain size distributions at the material points 1, 2, and 3 predicted by the FCE experiment and FEMCA-dDRX simulation.

## 5. Conclusions

1. In this study, a new MCA-dDRX model was proposed. In this model, the essential characteristics of dDRX were described by considering effective recrystallization nucleation and grain growth. It provides a more physical way of understanding the origin of oscillation of flow stress during dDRX.
2. Effects of the initial grain size on the kinetics of dDRX and flow behavior were highlighted. It is suggested a smaller initial grain size offers sufficient grain boundary cells as potential nucleation sites.
3. By integrating the proposed MCA-dDRX model into the FE simulation framework, the intrinsic mechanisms of large plastic deformation at non-uniform, non-isothermal, and varying strain rates were reasonably revealed. By comparing the simulation results with the metallurgical principles and the results of hot extrusion experiments, it was proved that the developed numerical simulation framework was capable of predicting the grain evolution of materials with a complex deformation history.
4. The proposed MCA model with sub-level cells can explain subgrain formation andLAGB migration during hot working. Due to this ability of the proposed model, it is beneficial to apply the modeling idea of the present simulation framework in highstacking-fault energy materials by defining the corresponding switching rules.

## CRedit authorship contribution statement

**F. Chen:** Methodology, Visualization, Funding acquisition, Writing-original draft. **H.J. Zhu:** Investigation, Data curation, Writing-review. **W. Chen:** Methodology, Writing-review & editing. **H. Ou:** Methodology, Writing-review & editing. **Z.S. Cui:** Project administration, Funding acquisition, Methodology, Writing-review & editing.

## Acknowledgments

This work is supported by the National Natural Science Foundation of China (Grant Nos. 51705316 and U2037204).

## Appendix A-Modeling of 3D MCA

## Appendix A1-The key factors of 3D MCA

Figure A1 shows a schematic of the mesoscale 3D MCA modeling idea. The main idea of this model is to introduce the 3D von Neumann neighborhood into the entire cellular space in the MCA simulation framework to efficiently simulate the equiaxed growth of recrystallized grains. Figure A1 also shows the application of the von Neumann neighborhood in the 3D MCA model.

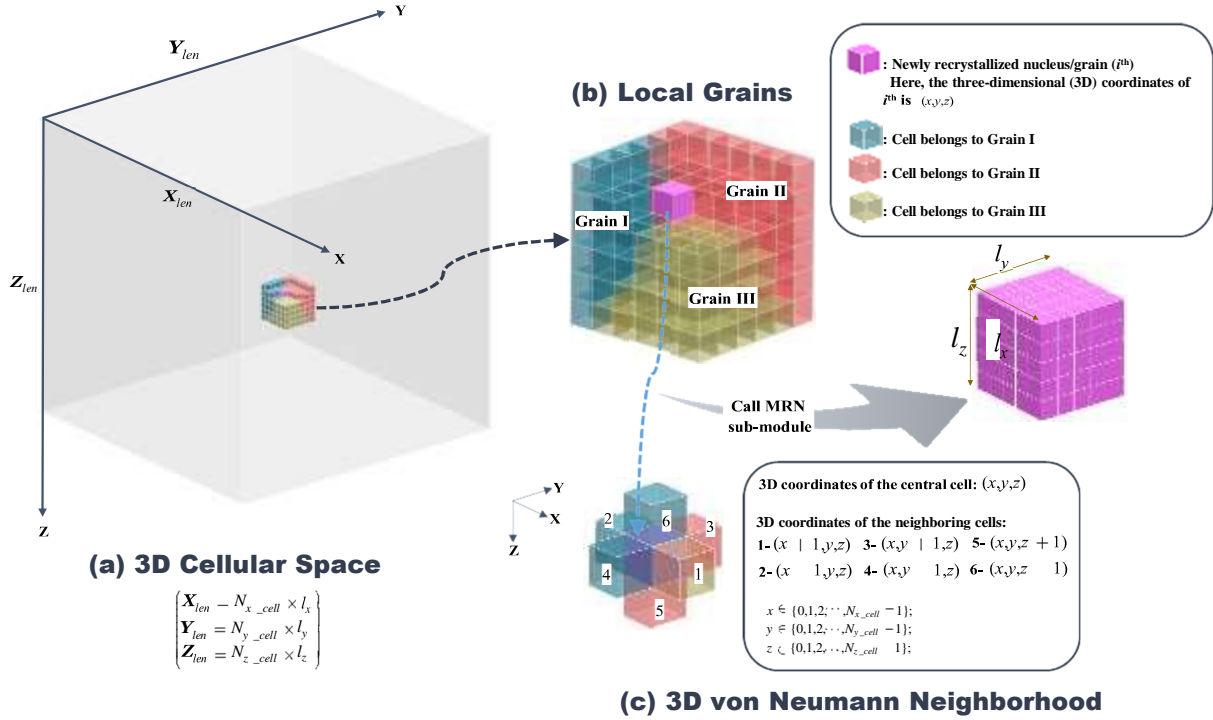


**Fig. A1.** Schematic of the mesoscale MCA modeling idea. In the current simulation, the size of the sub-potential nucleus was set as a cube with the edge length of  $l_0=10$  nm, and the number of sub-cells in the potential nucleus was calculated by  $\left(\frac{l_x}{l_0} \times \frac{l_y}{l_0} \times \frac{l_z}{l_0}\right)$ .

As shown in Fig. A1a, the initial cellular space was set as  $50 \times 50 \times 50$ , corresponding to the computation volume of  $100 \times 100 \times 100 \mu\text{m}^3$  in the real deformed billet. This means that  $N_{x\_cell} = N_{y\_cell} = N_{z\_cell} = 50$  and  $l_x = l_y = l_z = s_0 = 2 \mu\text{m}$ . The cells present on the border of the 3D cellular space inevitably lose some of their neighboring cells (Ding and Guo, 2001; Chen et al., 2009); to effectively solve this problem, periodic boundary conditions (PBCs) were employed to reduce the interface effects. For example, the cells located on the  $\langle \mathbf{Y} = 49 \rangle$  surface have their neighboring cells located on the  $\langle \mathbf{Y} = 0 \rangle$  surface. To accurately reflect the physical metallurgy principles of recrystallization nucleation, the MRN module is set up to describe the formation of effective nuclei when the critical condition of dDRX is reached. Before the potential nucleus in the parent cellular space is discretized in time and space, the cells present at the grain boundaries (including primary boundaries and newly recrystallized grain boundaries) are identified. In this study, dual-layer cells were recognized as the grain boundaries. The process of determining whether a cell with the  $(x,y,z)$  coordinates is located

at the grain boundaries is as follows: the orientation of the cell with the  $(x - 1, y, z)$  coordinates is different from that of the cell with the  $(x + 1, y, z)$  coordinates. This judgment criterion is also equally applicable to the other two directions.

As shown in Fig. A1b, the cell with the  $(x, y, z)$  coordinates (marked by pink color) was randomly selected as a potential recrystallized nucleus. The dislocation density of the cell must be higher than the critical value calculated by Eq. (9). Moreover, the cell should be located at the grain boundaries. Then, the MRN module is set up to determine the final state (an effective nucleus/cell or an ineffective nucleus/cell) of the potential nucleus that is discretized into a sub/multilevel cellular space.

The next important issue is to simulate the growth of the effective nucleus. As shown in Fig. A1c, the von Neumann neighborhood provides the closest cells to the central nucleus/cell with the  $(x, y, z)$  coordinates. When the cell recrystallizes, the dislocation density

of the cell is set to  $\rho_{initial}$ . The difference between the dislocation densities of the recrystallized cell and its closest neighbors offers the driving force for the subsequent grain growth. The nucleus can reach a stable state by consuming the original grains/cells around it, following the model of equiaxed growth. For example, Fig. A1c comprehensively depicts the coordinates of the six closest neighbors of the cell with  $(x, y, z)$  coordinates. Within the MCA time step defined by Eq. (15), the driving forces between the central cell and its six closest neighbors were calculated according to  $F_{\beta} = \tau(\rho_{matrix} - \rho_i) - \frac{2\gamma_{\beta}}{r_i}$ . If  $F_{\beta} > 0$ , the recrystallized

fraction state variable of the neighboring cells is updated cumulatively.

Another important component of the MCA model is the cellular state switching rules, which control whether recrystallization would occur in the neighboring cells. Based on the thermodynamic mechanism and the activation energy and considering the effect of the curvature-driven mechanism, the control state switching rules have been established as follows: (1) The driving force is positive. If more than one neighboring recrystallized cell consumes the same cell within a CA time step, the driving forces are individually evaluated and then compared. As a result, the cell with the maximum force will win the competition. (2)

The recrystallized fraction state variable calculated by  $f_{\beta}^t = \frac{l_{\beta}^t}{s_0} = \frac{(l_{\beta}^{t-\Delta t} + v_{\beta}\Delta t)}{s_0}$  is

equal to 1. Figure A2 shows the detailed implementation process of updating the recrystallized fraction variable of the neighboring cells during the growth of a newly recrystallized nucleus/grain. (3) The cell is located at the grain boundary, and simultaneously, there is at least one cell in its von Neumann neighborhood, which is already in the recrystallized state. (4) As is commonly known, the most significant feature of a CA model is the probability control method, which was explained for the first time by a pioneer in the field named Conway's Game of Life. In this study, the state transformation probability  $P_i$  depends only on the number  $i$  of neighboring cells, which have a higher dislocation density

when compared with that of the cell waiting for state transformation. If  $N_i / 100$  ( $N_i$  is the generated random number from 0 up to 100) is less than  $P_i = \bar{\omega}_i / 6$ , the state transformation occurs.

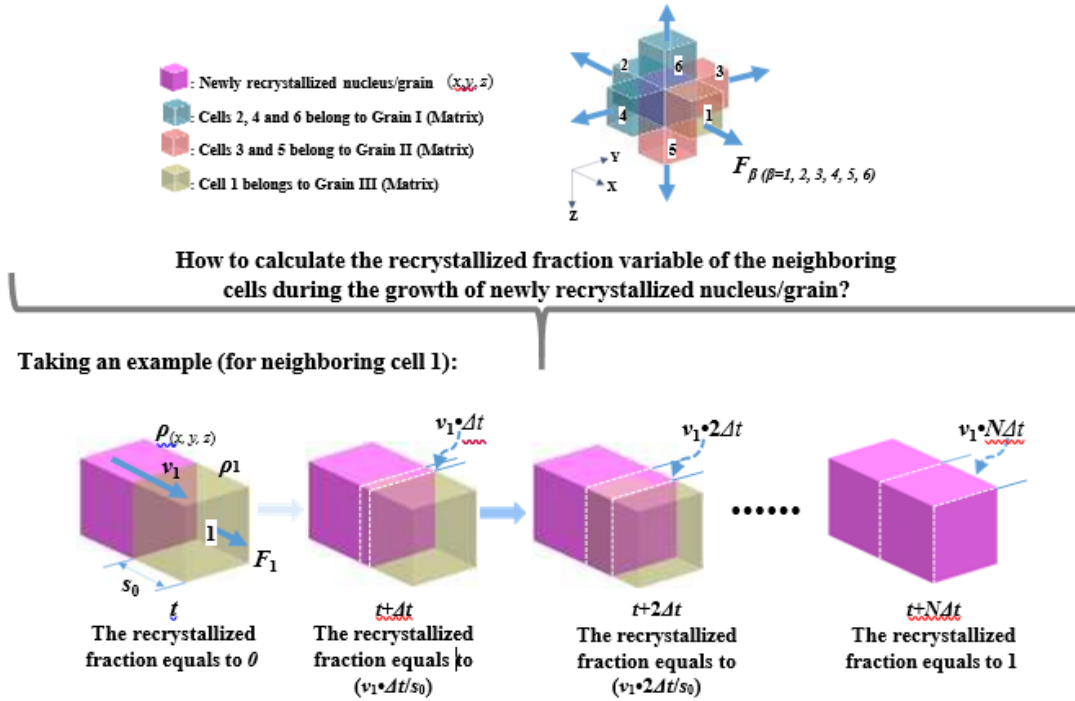


**Fig. A2.** Schematic of calculating the recrystallized fraction variable of neighboring cells during the equiaxed growth of the nucleus/grain.

In the MCA model, to calculate the physical fields and further update the crystallographic information during hot working, state variables of the cell are extensively used to quantify the features of microstructure evolution. In this study, each cell has seven state variables: (1) the dislocation density variable  $\rho_i$  that represents the stored energy. The initial dislocation density of all primary grains is uniform and identical. When recrystallization occurs in a cell, the dislocation density is set to  $\rho_{initial}$ , and then, the dislocation multiplication with an increase in strain is measured according to Eq. (1); (2) The grain orientation variable  $Q_i$  that represents different grains and can also be used to calculate  $\gamma_\beta$  according to Eq. (10); (3) The grain boundary variable that indicates whether the cell is located at the grain boundary; (4) The fraction variable  $f_i^t$  that represents the recrystallized fraction; (5) The grain size variable  $r_i$  that implies the recrystallized grain size, which can be updated according to Eq. (14); (6) Grain number that quantifies the number of grains in the simulated volume of the material point. Its value is increased by one when an effective nucleus is formed, which ensures that each grain has a unique number. Noted that the real grain number in the

simulated volume is substantially lower than the accumulated value due to the consumption of grains in the matrix; and (7) The number of recrystallization cycles that provide the sequence of dDRX. Its value is increased by one when effective nuclei are formed within an MCA time step. This means that the nuclei in the same recrystallization cycle demonstrate the same priority in the following grain growth competition.

#### Appendix A2-Details of the calculation of $\rho_{critical}$ for dDRX

Without loss of generality, a spherical nucleus with the radius  $r$  is introduced. As shown in Fig. A3a, the difference between the dislocation densities offers the driving force for grain boundary migration. The difference between the stored energies ( $\Delta E$ ) can be calculated using Eq. (A1).

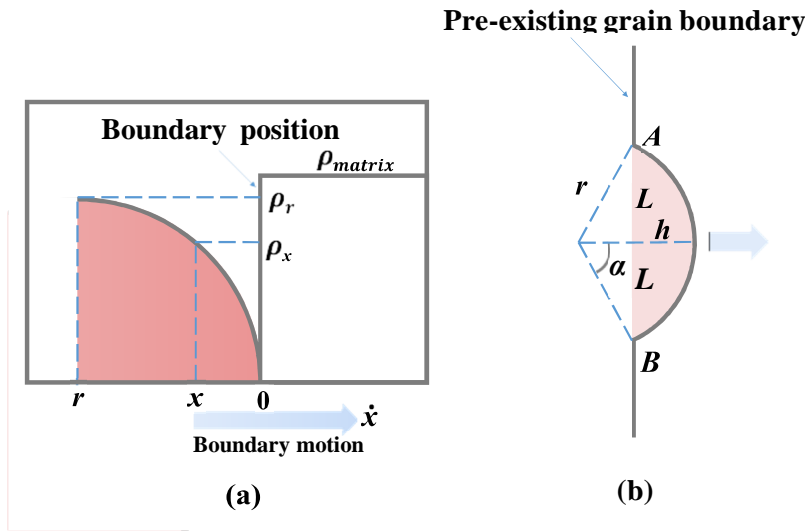


**Fig. A3.** (a) Schematic of dislocation density evolution at a dDRX front. (b) Schematic of the bulging nucleation mechanism of pre-existing grain boundaries during dDRX. (Roberts and Ahlblom, 1978) (Reproduced with permission from Elsevier)

$$\Delta E = \frac{\tau}{r} \int_0^r (\rho_{matrix} - \rho(x)) dx \quad (A1)$$

where  $\tau$  is the dislocation line energy. The net free energy change is presented as follows:

$$\Delta G(r) = -\frac{4}{3} \pi r^3 \frac{\tau}{r} \int_0^r (\rho_{matrix} - \rho(x)) dx + 4\pi r^2 \gamma_\beta \quad (A2)$$

As shown in Fig. A3b, the bulge mechanism can be represented by the following expression corresponding to Eq. (A2):

$$\Delta G(r) = -\frac{1}{3} \pi \frac{L^3 \sin^2 \alpha}{1 + \cos \alpha} \left( \frac{3}{\sin \alpha} - \frac{\sin \alpha}{1 + \cos \alpha} \right) \frac{\tau}{r} \int_0^r (\rho_{matrix} - \rho(x)) dx + \frac{2\pi L^2 \gamma_i}{1 + \cos \alpha} - \pi L^2 \gamma_\beta \quad (A3)$$

where  $r = \frac{L \sin \alpha}{1 + \cos \alpha}$ . By neglecting the effects of DRV, the dislocation density can be calculated as follows:

$$\frac{d\rho}{dt} = \frac{\dot{\varepsilon}}{bl} \quad (\text{A4})$$

where  $b$  is the Burgers vector, and  $l$  is the average mean free path of the mobile dislocation. Furthermore, the grain boundary migration can be expressed by

$$\frac{dx}{dt} = v = M\tau(\rho_{matrix} - \rho(x=0)) \approx M\tau\rho_{matrix} \quad (\text{A5})$$

where  $M$  is the grain boundary mobility. By combining Eq. (A5) and Eq. (A6) and ignoring the sign of  $x$ , we obtain

$$\rho(x) = \frac{\dot{\varepsilon}}{blM\tau\rho_{matrix}}x \quad (\text{A6})$$

By combining of Eq. (A7) and Eq. (A3) followed by differentiation to find maxima in  $\Delta G(r)$ , we acquire

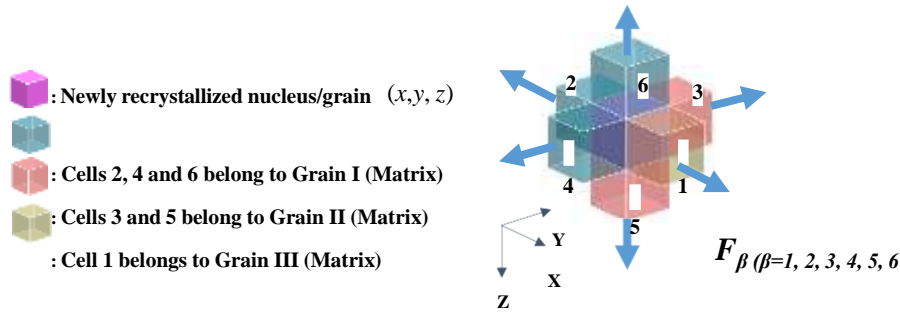
$$L^2 \frac{\dot{\varepsilon}}{blM\tau\rho_{matrix}} \left( \frac{5 + \cos\alpha}{1 + \cos\alpha} \right) \sin\alpha - L \tau\rho_{matrix} + 2\gamma_{\beta} \sin\alpha = 0 \quad (\text{A7})$$

which provides the real critical size  $L_{critical}$  only if

$$\rho_{critical} \geq \left( \frac{20\dot{\varepsilon}\gamma_{\beta}}{3blM\tau^2} \right)^{1/3} \quad (\text{A8})$$

### Appendix A3-Details for the calculation of misorientation

As shown in Fig. A4, six neighboring cells belong to three different grains (I, II and III) around the newly recrystallized grain (orientation\_0) marked by pink. Hereinafter, the method to calculate the misorientation for this case is presented.



### How to calculate the misorientation during the growth of newly recrystallized nucleus/grain?

- ✓  $\Theta_1 = \text{abs}(\text{Orientation}_0 - \text{Orientation}_1)$
- ✓  $\Theta_3 = \Theta_5 = \text{abs}(\text{Orientation}_0 - \text{Orientation}_3) = \text{abs}(\text{Orientation}_0 - \text{Orientation}_5)$
- ✓  $\Theta_2 = \Theta_4 = \Theta_6 = \text{abs}(\text{Orientation}_0 - \text{Orientation}_2) = \text{abs}(\text{Orientation}_0 - \text{Orientation}_4) = \text{abs}(\text{Orientation}_0 - \text{Orientation}_6)$

**Fig. A4.** Schematic of calculating the misorientation by MCA.

#### Appendix B- Data transfer from FE to MCA

During multiscale modeling of dDRX, the local physical fields are calculated at every node via the governing equation by FE on the macroscale. The thermal and deformation histories in terms of temperature, effective strain rate, and strain are provided as input to the MCA simulation on the mesoscale. In other words, MCA can be understood as the FE post-processing technique.

The FE time increment always occurs at a different level of MCA time increment. Normally, the FE time increment has to be discretized according to the MCA time increment such that MCA can be applied to non-uniform and non-isothermal processes. According to Eqs. (7) and (15), the updated MCA time increment can be measured as follows:

$$\Delta t_i = \frac{d_0}{2} \left[ \frac{\mu_0 \left[ 1 - 0.91 \times \left( \frac{T_i - 300}{T_m} \right) \right]}{\frac{\delta D_{ob} b}{KT_i} \exp \left( -\frac{Q_b}{RT} \right) \sigma_{saturation}^2} \right] \quad (B1)$$

As an example, Fig. B1 shows the coupled computation of meso- and macro- physical fields. Via FE simulation, the physical fields of the  $i^{th}$  step were recorded, and then introduced into Eq. (B1); this afforded the time increment of MCA simulation from the  $(i - 1)^{th}$  step to the  $i^{th}$  step under the condition of strain increment  $\Delta \tilde{\epsilon}^{(i-1) \rightarrow i}$  can be obtained. Subsequently, the number of MCA simulation steps corresponding to a time increment of FE was evaluated by

$$N_{i\_num\_MCA} = \frac{\Delta \tilde{\epsilon}^{(i-1) \rightarrow i}}{\tilde{\epsilon}^{(i-1)} \Delta t_i} \quad (B2)$$

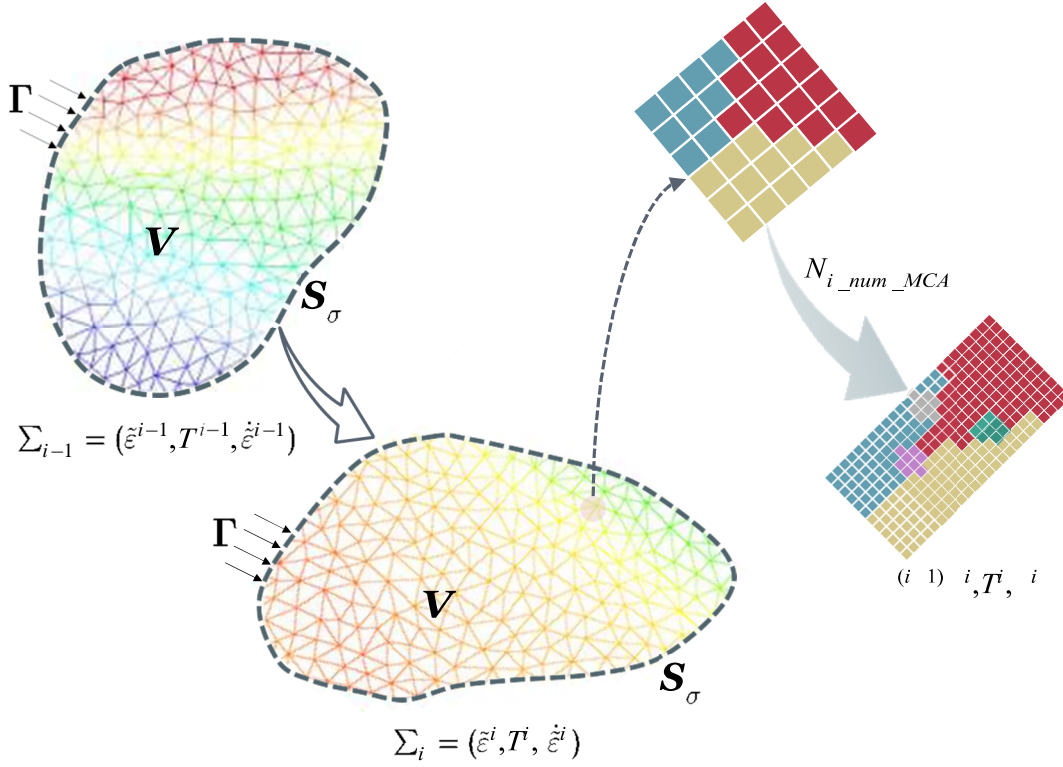


**Fig. B1.** Schematic diagram of the meso- and macro- computational simulation framework. Here  $\mathbf{V}$  is the volume,  $\mathbf{S}_\sigma$  is the surface, and  $\Gamma$  means the boundary conditions in the governing equations of FE simulation.  $\Sigma_{i-1} = (\tilde{\epsilon}^{i-1}, T^{i-1}, \dot{\tilde{\epsilon}}^{i-1})$  and  $\Sigma_i = (\tilde{\epsilon}^i, T^i, \dot{\tilde{\epsilon}}^i)$  are the physical fields for the  $(i-1)^{th}$  and  $i^{th}$  FE steps, respectively;  $N_{i\_num\_MCA}$  is the number of MCA steps accordingly;  $\Omega = [\Delta\tilde{\epsilon}^{(i-1)\rightarrow i}, T^i, \dot{\tilde{\epsilon}}^i]$  provides the governing macro-physical parameters of the mesoscale simulation. A section of a meshed billet with tetrahedron elements was employed as an example.

To improve the calculation efficiency, it is not necessary to frequently update  $\Delta t_i$ . A threshold value should be defined to estimate when the  $\Delta t_i$  value should be adjusted. Herein, if the increase/decrease in the  $\Delta t_i$  value exceeds 10% of the value in the previous step, the strain rate and temperature are updated accordingly. This suggests that  $k_1$  of Eq. (1),  $\rho_{critical}$  of Eq. (9), and  $\dot{n}_{dDRX}$  of Eq. (12) are also correspondingly updated owing to the change in the effective strain rate and temperature.

### Declaration of interests

The authors declare that they have no known competing financial interests or personal relationships that could have appeared to influence the work reported in this paper.

## Author statement

**F. Chen:** Methodology, Visualization, Funding acquisition, Writing-original draft. **H.J. Zhu:** Investigation, Data curation, Writing-review. **W. Chen:** Methodology, Writing-review & editing. **H. Ou:** Methodology, Writing-review & editing. **Z.S. Cui:** Project administration, Funding acquisition, Methodology, Writing-review & editing.

## References

- Andrade-Campos, A., Thuillier, S., Pilvin, P., Teixeira-Dias, F., 2007. On the determination of material parameters for internal variable thermoelastic-viscoplastic constitutive models. *Int. J. Plasticity* 23, 1349-1379. <https://doi.org/10.1016/j.ijplas.2006.09.002>.
- Bailey, J.E., Hirsch, P.B., 1960. The dislocation distribution, flow stress, and stored energy in cold-worked polycrystalline silver. *Philos. Mag.* 5 (53), 485-497. <https://doi.org/10.1080/14786436008238300>.
- Blaz, L., Sakai, T., Jonas, J.J., 1983. Effect of initial grain size on dynamic recrystallization of copper. *Metal Sci.* 17, 609-616. <https://doi.org/10.1179/030634583790420448>.
- Busso, E.P., 1998. A continuum theory for dynamic recrystallization with microstructure-related length scales. *Int. J. Plasticity* 14, 319-353. [https://doi.org/10.1016/S0749-6419\(98\)00008-4](https://doi.org/10.1016/S0749-6419(98)00008-4).
- Calamaz, M., Coupard, D., Girod, F., 2008. A new material model for 2D numerical simulation of serrated chip formation when machining titanium alloy Ti-6Al-4V. *Int. J. Mach. Tools. Manf.* 48, 275- 288. <https://doi.org/10.1016/j.ijmactools.2007.10.014>.
- Chatziathanasiou, D., Chemisky, Y., Chatzigeorgiou, G., Meraghni, F., 2016. Modeling of coupled phase transformation and reorientation in shape memory alloys under non-proportional thermomechanical loading. *Int. J. Plasticity* 82, 192-224. <https://doi.org/10.1016/j.ijplas.2016.03.005>.
- Chen, F., Cui, Z.S., Liu, J., Zhang, X.X., Chen, W., 2009. Modeling and simulation on dynamic recrystallization of 30Cr2Ni4MoV rotor steel using the cellular automaton method. *Modelling Simul. Mater. Sci. Eng.* 17, 075015. doi:10.1088/0965-0393/17/7/075015.
- Chen, F., Cui, Z.S., Liu, J., Chen, W., Chen, S.J., 2010. Mesoscale simulation of the high-temperature austenitizing and dynamic recrystallization by coupling a cellular automaton with a topology deformation technique. *Mater. Sci. Eng. A* 527, 5539-5549. <https://doi.org/10.1016/j.msea.2010.05.021>.
- Chen, F., Cui, Z.S., 2012. Mesoscale simulation of microstructure evolution during multi-stage hot forging processes. *Modelling Simul. Mater. Sci. Eng.* 20, 045008. doi:10.1088/0965-0393/20/4/045008.
- Chen, F., Qi, K., Cui, Z.S., Lai, X.M., 2014. Modeling the dynamic recrystallization in austenitic stainless steel using cellular automaton method. *Comp. Mater. Sci.* 83, 331-340. <https://doi.org/10.1016/j.commatsci.2013.11.029>.
- Chen, F. Zhu, H.J., Zhang, H.M., Cui, Z.S., 2020. Mesoscale modeling of dynamic recrystallization: Multilevel cellular automaton simulation framework. *Metall. Mater. Trans. A* 51, 1286-1303. <https://doi.org/10.1007/s11661-019-05620-3>.
- Chen, M.S., Lin, Y.C., 2013. Numerical simulation and experimental verification of void evolution inside large forgings during hot working. *Int. J. Plasticity* 49, 53-70. <https://doi.org/10.1016/j.ijplas.2013.02.017>.
- Cho, H.E., Hammi, Y., Bowman, A.L., Karato, S., Baumgardner, J.R., Horstemeyer, M.F., 2019. A unified static and dynamic recrystallization Internal State Variable (ISV) constitutive model coupled with grain size evolution for metals and mineral aggregates. *Int. J. Plasticity* 112, 123-157. <https://doi.org/10.1016/j.ijplas.2018.08.009>.
- Ding, R., Guo, Z.X., 2001. Coupled quantitative simulation of microstructural evolution and plastic flow during dynamic recrystallization. *Acta Mater.* 49, 3163-3175. [https://doi.org/10.1016/S1359-6454\(01\)00233-6](https://doi.org/10.1016/S1359-6454(01)00233-6).
- Doherty, R., Hughes, D.A., Humphreys, F., Jonas, J., Jensen, D.J., Kassner, M., King, W., McNelley, T., McQueen, H., Rollett, A., 1997. Current issues in recrystallization: a review. *Mater. Sci. Eng. A* 238, 219-274. [https://doi.org/10.1016/S0921-5093\(97\)00424-3](https://doi.org/10.1016/S0921-5093(97)00424-3).

Fan, X.G., Yang, H. 2011. Internal-state-variable based self-consistent constitutive modeling for hotworking of two-phase titanium alloys coupling microstructure evolution. *Int. J. Plasticity* 27, 1833-1852. <https://doi.org/10.1016/j.ijplas.2011.05.008>.

García, V., Cabrera, J., Riera, L., Prado, J., 2000. Hot deformation of a commercial purity copper. In: *Proceedings of Euromat 2000: Advances in Mechanical Behaviour, Plasticity and Damage*. Elsevier Science, Oxford, pp. 1357-1362.

Galiyev, A., Kaibyshev, R., Gottstein, G., 2001. Correlation of plastic deformation and dynamic recrystallization in magnesium alloy ZK60. *Acta Mater.* 49, 1199-1207. [https://doi.org/10.1016/S1359-6454\(01\)00020-9](https://doi.org/10.1016/S1359-6454(01)00020-9).

Ghazi, N., Niordson, C.F., Kysar, J.W., 2018. Plastic strain recovery in nanocrystalline copper thin films. *Int. J. Plasticity* 107, 27-53. <https://doi.org/10.1016/j.ijplas.2018.03.010>.

Goetz, R.L., Seetharaman, V., 1998. Modeling dynamic recrystallization using cellular automata. *Scripta Mater.* 38, 405-413. [https://doi.org/10.1016/S1359-6462\(97\)00500-9](https://doi.org/10.1016/S1359-6462(97)00500-9).

Gourdet, S., Montheillet, F., 2003. A model of continuous dynamic recrystallization. *Acta Mater.* 51, 2685-2699. [https://doi.org/10.1016/S1359-6454\(03\)00078-8](https://doi.org/10.1016/S1359-6454(03)00078-8).

He, Y.Y., Bai, S.W., Fang, G., 2020. Coupled CA-FE simulation for dynamic recrystallization of magnesium alloy during hot extrusion. *J. Magnes. Alloy.* 14:45. <https://doi.org/10.1016/j.jma.2020.08.023>.

Huang, K., Logé, R.E., 2016. A review of dynamic recrystallization phenomena in metallic materials. *Mater. Des.* 11, 548-574. <https://doi.org/10.1016/j.matdes.2016.09.012>.

Huang, K., Marthinsen, K., Zhao, Q.L., Logé, R.E., 2018. The double-edge effect of second-phases on the recrystallization behaviour and associated mechanical properties of metallic materials. *Prog. Mater. Sci.* 92, 284-359. <https://doi.org/10.1016/j.pmatsci.2017.10.004>.

Janssens, K.G.F., 2003. Random grid, three-dimensional, space-time coupled cellular automata for the simulation of recrystallization and grain growth. *Modell. Simul. Mater. Sci. Eng.* 11, 157-171.

Janssens, K.G.F., 2010. An introductory review of cellular automata modeling of moving grain boundaries in polycrystalline materials. *Math. Comput. Simul.* 80, 1361-1381. <https://doi.org/10.1016/j.matcom.2009.02.011>.

Jin, Z.Y., Cui, Z.S., 2010. Investigation on strain dependence of dynamic recrystallization behavior using an inverse analysis method. *Mater. Sci. Eng. A* 527, 3111-3119. <https://doi.org/10.1016/j.msea.2010.01.062>.

Jonas, J.J., Queleñec, X., Jiang, L., Martin É., 2009. The Avrami kinetics of dynamic recrystallization. *Acta Mater.* 57, 2748-2756. <https://doi.org/10.1016/j.actamat.2009.02.033>.

Lieou, C.K.C., Bronkhorst, C.A., 2018. Dynamic recrystallization in adiabatic shear banding: Effective-temperature model and comparison to experiments in ultrafine-grained titanium. *Int. J. Plasticity* 111, 107-121. <https://doi.org/10.1016/j.ijplas.2018.07.011>.

Kassner, M.E., Barrabes, S.R., 2005. New developments in geometric dynamic recrystallization. *Mater. Sci. Eng. A* 410-411, 152-155. <https://doi.org/10.1016/j.msea.2005.08.052>.

Konijnenberg, P.J., Zaefferer, S., Raabe, D., 2015. Assessment of geometrically necessary dislocation levels derived by 3D EBSD. *Acta Mater.* 99, 402-414. <https://doi.org/10.1016/j.actamat.2015.06.051>.

Kugler, G., Turk, R., 2004. Modeling the dynamic recrystallization under multi-stage hot deformation. *Acta Mater.* 52, 4659-4668. <https://doi.org/10.1016/j.actamat.2004.06.022>.

Lee, H.W., Im, Y.-T., 2010. Numerical modeling of dynamic recrystallization during nonisothermal hot compression by cellular automata and finite element analysis. *Int. J. Mech. Sci.* 52, 1277-1289. <https://doi.org/10.1016/j.ijmecsci.2010.06.003>.

Lieou, C.K.C., Mourad, H.M., Bronkhorst, C.A., 2019. Strain localization and dynamic recrystallization in polycrystalline metals: Thermodynamic theory and simulation framework. *Int. J. Plasticity* 119, 171-187. <https://doi.org/10.1016/j.ijplas.2019.03.005>.

Lin, J., Liu, Y., 2003. A set of unified constitutive equations for modelling microstructure evolution in hot deformation. *J. Mater. Process. Technol.* 143-144, 281-285. [https://doi.org/10.1016/S0924-0136\(03\)00472-2](https://doi.org/10.1016/S0924-0136(03)00472-2).

Lin, J., Dean, T.A., 2005. Modelling of microstructure evolution in hot forming using unified constitutive equations. *J. Mater. Process. Tech.* 30, 354-362. <https://doi.org/10.1016/j.jmatprotec.2005.06.026>.

Lin, Y.C., Chen, M.S., Zhong, J., 2008. Numerical simulation for stress/strain distribution and microstructural evolution in 42CrMo steel during hot upsetting process. *Comput. Mater. Sci.* 43, 1117-1122. <https://doi.org/10.1016/j.commatsci.2008.03.010>.

Li, H., Sun, X., Yang, H., 2016. A three-dimensional cellular automata-crystal plasticity finite element model for predicting the multiscale interaction among heterogeneous deformation, DRX microstructural evolution and mechanical response in titanium alloys. *Int. J. Plasticity* 2016, 154-180. <https://doi.org/10.1016/j.ijplas.2016.09.008>.

Manonukul, A., Dunne, F., 1999. Initiation of dynamic recrystallization under inhomogeneous stress states in pure copper. *Acta Mater.* 47, 4339-4354. [https://doi.org/10.1016/S1359-6454\(99\)00313-4](https://doi.org/10.1016/S1359-6454(99)00313-4).

McQueen, H.J., 2004. Development of dynamic recrystallization theory. *Mater. Sci. Eng. A* 387-389, 203-208. <https://doi.org/10.1016/j.msea.2004.01.064>.

Miura, H., Sakai, T., Hamaji, H., Jonas, J.J., 2004. Preferential nucleation of dynamic recrystallization at triple junctions. *Scripta Mater.* 50, 65-69. <https://doi.org/10.1016/j.scriptamat.2003.09.035>.

Nagra, J.S., Brahme, A., Lebensohn, R.A., Inal, K., 2017. Efficient fast Fourier transform-based numerical implementation to simulate large strain behavior of polycrystalline materials. *Int. J. Plasticity* 98, 65-82. <https://doi.org/10.1016/j.ijplas.2017.07.001>.

Nagra, J.S., Brahme, A., Mishra, R., Lebensohn, R.A., Inal, K., 2018. An efficient full-field crystal plasticity-based M-K framework to study the effect of 3D microstructural features on the formability of polycrystalline materials. *Model. Simul. Mater. Sci. Eng.* 26, 075002. <https://doi.org/10.1088/1361-651X/aadc20>.

Nagra, J.S., Brahme, A., Lévesque, J., Mishra, R., Lebensohn, R.A., Inal, K., 2020. A new micromechanics full field numerical framework to simulate the effects of dynamic recrystallization on the formability of HCP metals. *Int. J. Plasticity* <https://doi.org/10.1016/j.ijplas.2019.09.011>.

Nicolaÿ, A., Fiorucci, G., Franchet, J.M., Cormier, J., Bozzolo, N., 2019. Influence of strain rate on subsolvus dynamic and post-dynamic recrystallization kinetics of Inconel 718. *Acta Mater.* 174, 406-417. <https://doi.org/10.1016/j.actamat.2019.05.061>.

Peczak, P., Luton, M. J., 1993. The effect of nucleation models on dynamic recrystallization I. Homogeneous stored energy distribution. *Philos. Mag. Part B*, 68, 115-144. <https://doi.org/10.1080/01418639408240254>.

Peczak, P., Luton, M. J., 1994. The effect of nucleation models on dynamic recrystallization II. Heterogeneous stored-energy distribution. *Philos. Mag. Part B*, 70, 817-849. <https://doi.org/10.1080/13642819308215285>.

Poliak, E., Jonas, J., 2003. Initiation of dynamic recrystallization in constant strain rate hot deformation. *ISIJ Int.* 43, 684-691. <https://doi.org/10.2355/isijinternational.43.684>.

Ponge, D., Gottstein, G., 1998. Necklace formation during dynamic recrystallization: mechanisms and impact on flow behaviour. *Acta Mater.* 46, 69-80. [https://doi.org/10.1016/S1359-6454\(97\)00233-4](https://doi.org/10.1016/S1359-6454(97)00233-4).

Popova, E., Staraselski, Y., Brahme, A., Mishra, R.K., Inal, K., 2015. Coupled crystal plasticity-Probabilistic cellular automata approach to model dynamic recrystallization in magnesium alloys. *Int. J. Plasticity* 66, 85-102. <https://doi.org/10.1016/j.ijplas.2014.04.008>.

Popova, E., Brahme, A.P., Staraselski, Y., Agnew, S.R., Mishra, R.K., Inal, K., 2016. Effect of extension {1012} twins on texture evolution at elevated temperature deformation accompanied by dynamic recrystallization. *Mater. Des.* 96, 446-457. <https://doi.org/10.1016/j.matdes.2016.02.042>.

Puchi-Cabrera, E.S., Staia, M.H., Guérin, J.D., Lesage, J., Dubar, M., Chicot, D. 2013. Analysis of the work-hardening behavior of C-Mn steels deformed under hot-working conditions. *Int. J. Plasticity* 51, 145-160. <https://doi.org/10.1016/j.ijplas.2013.05.007>.

Puchi-Cabrera, E.S., Staia, M.H., Guérin, J.D., Lesage, J., Dubar, M., Chicot, D. 2014. An experimental analysis and modeling of the work-softening transient due to dynamic recrystallization. *Int. J. Plasticity* 54, 113-131. <https://doi.org/10.1016/j.ijplas.2013.08.011>.

Puchi-Cabrera, E.S., Guérin, J.D., La Barbera-Sosa, J.G., Dubar, M., Dubar, L. 2018. Plausible extension of Anand's model to metals exhibiting dynamic recrystallization and its experimental validation. *Int. J. Plasticity* 108, 70-87. <https://doi.org/10.1016/j.ijplas.2018.04.013>.

Qu, J., Jin, Q.L., Xu, B.Y., 2005. Parameter identification for improved viscoplastic model considering dynamic recrystallization. *Int. J. Plasticity* 21, 1267-1302. <https://doi.org/10.1016/j.ijplas.2004.04.009>.

Qu, J., Jin, Q.L., Xu, B.Y., 2008. Parameter identification of superplastic constitutive model by GA-based global optimization method. *J. Mater. Process. Technol.* 197, 212-220. <https://doi.org/10.1016/j.jmatprotec.2007.06.011>.

Raabe, D., 1999. Introduction of a scalable three-dimensional cellular automaton with a probabilistic switching rule for the discrete mesoscale simulation of recrystallization phenomena. *Philos. Mag. A* 79, 2339-2358. [doi:10.1080/01418619908214288](https://doi.org/10.1080/01418619908214288).

Raabe, D., Becker, R.C., 2000. Coupling of a crystal plasticity finite element mode with a probabilistic cellular automaton for simulating primary static recrystallization in aluminium. *Modell. Simul. Mater. Sci. Eng.* 8, 445. <https://doi.org/10.1002/3527606157.ch1>.

Raabe, D., 2002 Cellular automata in materials science with particular reference to recrystallization simulation. *Annu. Rev. Mater. Sci.* 32, 53-76. doi:10.1146/annurev.matsci.32.090601.152855.

Reuber, C., Eisenlohr, P., Roters, F., Raabe, D., 2014. Dislocation density distribution around an indent in single-crystalline nickel: Comparing nonlocal crystal plasticity finite-element predictions with experiments. *Acta Mater.* 71, 333-348. <https://doi.org/10.1016/j.actamat.2014.03.012>.

Rollett, A., Humphreys, F., Rohrer, G.S., Hatherly, M., 2004. *Recrystallization and Related Annealing Phenomena*, second ed. Elsevier. *Recrystallization and Related Annealing Phenomena: Second Edition*.

Rossard, C., Blain, P., 1959. Evolution of steel microstructure during plastic deformation at high temperature. *Mem. Sci. Rev. Metall.* 56, 285-298.

Roters, F., Raabe, D., Gottstein, G., 2000. Work hardening in heterogeneous alloys—a microstructural approach based on three internal state variables. *Acta Mater.* 48, 4181-4189. [https://doi.org/10.1016/S1359-6454\(00\)00289-5](https://doi.org/10.1016/S1359-6454(00)00289-5).

Sakai, T., Belyakov, A., Kaibyshev, R., Miura, H., Jonas, J.J., 2014. Dynamic and post-dynamic recrystallization under hot, cold and severe plastic deformation conditions. *Prog. Mater. Sci.* 60, 130-207. <https://doi.org/10.1016/j.pmatsci.2013.09.002>.

Sellars, C.M., 1985. Computer modelling of hot-working processes. *Mater. Sci. Tech.* 1, 325-332. <https://doi.org/10.1179/mst.1985.1.4.325>.

Sellars, C.M., Zhu, Q., 2000. Microstructural modelling of aluminium alloys during thermomechanical processing. *Mater. Sci. Eng. A* 280, 1-7. [https://doi.org/10.1016/S0921-5093\(99\)00648-6](https://doi.org/10.1016/S0921-5093(99)00648-6).

Shahbaz, M., Pardis, N., Ebrahimi, R., Talebanpour, B., 2011. A novel single pass severe plastic deformation technique: Vortex extrusion. *Mater. Sci. Eng. A* 530, 469-472. <https://doi.org/10.1016/j.msea.2011.09.114>.

Shahbaz, M., Pardis, N., Kim, J.G., Ebrahimi, R., Kim, H.S., 2016. Experimental and finite element analyses of plastic deformation behavior in vortex extrusion. *Mater. Sci. Eng. A* 674, 472-479. <https://doi.org/10.1016/j.msea.2016.07.044>.

Spranghers, K., Vasilakos, I., Lecompte, D., Sol, H., Vantomme, J., 2014. Identification of the plastic behavior of aluminium plates under free air explosions using inverse methods and full-field measurements. *Int. J. Solids. Struct.* 51, 210-226. <https://doi.org/10.1016/j.ijsolstr.2013.09.027>.

Sun, Z.C., Wu, H.L., Cao, J., Yin, Z.K., 2018. Modeling of continuous dynamic recrystallization of Al-Zn-Cu-Mg alloy during hot deformation based on the internal-state-variable (ISV) method. *Int. J. Plasticity* 106, 73-87. <https://doi.org/10.1016/j.ijplas.2018.03.002>.

Svyetlichnyy, D.S., 2010. Modelling of the microstructure: from classical cellular automata approach to the frontal one. *Comput. Mater. Sci.* 50, 92-97. <https://doi.org/10.1016/j.commatsci.2010.07.011>.

Svyetlichnyy, D.S., 2014. A three-dimensional frontal cellular automaton model for simulation of microstructure evolution-initial microstructure module. *Model. Simul. Mater. Sci. Eng.* 22, 085001. doi:10.1088/0965-0393/22/8/085001.

Tang, T., Zhou, G.W., Li, Z.H., Li, D.Y., Peng, L.M., Peng, Y.H., Wu, P.D., Wang, M.H., Lee, M.-G., 2019. A polycrystal plasticity based thermos-mechanical-dynamic recrystallization coupled modeling method and its application to light weight alloys. *Int. J. Plasticity* 116, 159-191. <https://doi.org/10.1016/j.ijplas.2019.01.001>.

Takaki, T., Yoshimoto, C., Yamanaka, A., Tomita, Y., 2014. Multiscale modeling of hot-working with dynamic recrystallization by coupling microstructure evolution and macroscopic mechanical behavior. *Int. J. Plasticity* 52, 105-116. <https://doi.org/10.1016/j.ijplas.2013.09.001>.

Tsuzaki, K., Xiaoxu, H., Maki, T., 1996. Mechanism of dynamic continuous recrystallization during superplastic deformation in a microduplex stainless steel. *Acta Mater.* 44, 4491-4499. [https://doi.org/10.1016/1359-6454\(96\)00080-8](https://doi.org/10.1016/1359-6454(96)00080-8).

Wang, X.W., Wang, C.J., Liu, Y., Liu, C., Wang, Z.L., Guo, B., Shan, D.B., 2021. An energy based modeling for the acoustic softening effect on the Hall-Petch behavior of pure titanium in ultrasonic vibration assisted micro-tension. *Int. J. Plasticity* 136, 102879. <https://doi.org/10.1016/j.ijplas.2020.102879>.

Wu, C., Yang, H., Li, H., 2013. Modeling of discontinuous dynamic recrystallization of a near-alpha titanium alloy IMI834 during isothermal hot compression by combining a cellular automaton model with a crystal plasticity finite element method. *Comput. Mater. Sci.* 79, 944-959. <https://doi.org/10.1016/j.commatsci.2013.08.004>.

Xiao, N.M., Zheng, C.W., Li, D.Z., Li, Y.Y., 2008. A simulation of dynamic recrystallization by coupling a cellular automaton method with a topology deformation technique. *Comput. Mater. Sci.* 41, 366-374. <https://doi.org/10.1016/j.commatsci.2007.04.021>.

- Yang, H., Li, H., Ma, J., Wei, D., Chen, J., Fu, M.W., 2020. Temperature dependent evolution of anisotropy and asymmetry of  $\alpha$ -Ti in thermomechanical working: Characterization and modeling. *Int. J. Plasticity* 127, 102650. <https://doi.org/10.1016/j.ijplas.2019.102650>.
- Yazdipour, N., Davies, C.H.J., Hodgson, P.D., 2008. Microstructural modeling of dynamic recrystallization using irregular cellular automata. *Comput. Mater. Sci.* 44, 566-576. <https://doi.org/10.1016/j.commatsci.2008.04.027>.
- Zhang, J., Li, H.W., Sun, X.X., Zhan, M., 2020. A multi-scale MCCPFEM framework: Modeling of thermal interface grooving and deformation anisotropy of titanium alloy with lamellar colony. *Int. J. Plasticity* 135, 102804. <https://doi.org/10.1016/j.ijplas.2020.102804>.
- Zhao, P., Low, T.S.E., Wang, Y., Niezgoda, S.R., 2016. An integrated full-field model of concurrent plastic deformation and microstructure evolution: application to 3d simulation of dynamic recrystallization in polycrystalline copper. *Int. J. Plasticity* 80, 38-55. <https://doi.org/10.1016/j.ijplas.2015.12.010>.
- Zhao, P., Wang, Y., Niezgoda, S.R., 2018. Microstructural and micromechanical evolution during dynamic recrystallization. *Int. J. Plasticity* 100, 52-68. <https://doi.org/10.1016/j.ijplas.2017.09.009>.
- Zurob, H.S., Brchet, Y., Dunlop, J., 2006. Quantitative criterion for recrystallization nucleation in single-phase alloys: Prediction of critical strain and incubation times. *Acta Mater.* 54, 3983-3990. <https://doi.org/10.1016/j.actamat.2006.04.028>.